VON KARMAN INSTITUTE FOR FLUID DYNAMICS

LECTURE SERIES 1982-04

COMPUTATIONAL FLUID DYNAMICS

MARCH 29 - APRIL 2, 1982

RECENT DEVELOPMENTS IN FINITE-VOLUME TIME-DEPENDENT TECHNIQUES FOR TWO AND THREE DIMENSIONAL TRANSONIC FLOWS

WOLFGANG SCHMIDT, DORNIER GMBH, GERMANY

ANTONY JAMESON, PRINCETON UNIVERSITY, USA

Recent Developments in Finite-Volume Time-Dependent Techniques for Two- and Three-Dimensional Transonic Flows

Wolfgang Schmidt
Dornier GmbH
D-7990 Friedrichshafen

Antony Jameson
Princeton University
Princeton, NJ 08544

SUMMARY

Hyperbolic systems of partial differential equations governing inviscid and viscid flows are analyzed. A new combination of a finite volume discretization in conjunction with carefully designed dissipative terms, and Runge Kutta time stepping schemes, are shown to yield effective methods for solving the Euler equations in arbitrary geometric domains. Different types of acceleration techniques are discussed to improve convergence speed of explicit time dependent methods. Computational results ranging from viscid/inviscid airfoil flows to cascades, inlets, wings and wing-body configurations are presented. Special attention is given to the formulation of the Kutta condition and to flows with leading edge separation.

1. INTRODUCTION

Aircraft development costs have escalated exceedingly within the last years. Greater emphasis must be placed on exploring analytically and experimentally new configuration concepts aimed at substantially expanding airplane performance capabilities. The present state of the art in aerodynamic analysis and design requires extensive configuration iterations through repeated wind tunnel testing that is costly, time consuming, and relies heavily on

inhouse experiences and expertise. Significant advances have been achieved in the last few years in aerodynamic computational methods which allow the numerical computation of flows around three-dimensional configurations and provide valuable guides to those seeking understanding of specific problems or those pursuing innovative design concepts.

It is the purpose of this review to discuss some numerical techniques for solving hyperbolic systems of partial differential equations which govern flows which can be solved by time or space marching. For solutions for transonic potential flow which have been proved to be very useful, but are limited in application, Ref. 1-3 give good overviews. Here, the discussion is limited to solutions of the Euler and Navier Stokes equations. To solve problems numerically, one must make several decisions which include the following: the selection of an appropriate form of the equations which describe the flow of interest; an algorithm to calculate the numerical solution of the equations within a domain or region of the fluid; a technique to properly approximate boundary conditions along the boundaries of the domain; and finally, the treatment of shockwave discontinuities which may occur within the domain. For each of these decisions, useful, and in some cases promising, new alternatives will be presented and discussed.

2. GOVERNING SET OF DIFFERENTIAL EQUATIONS

Within the scope of this study we consider only flows governed by first-order hyperbolic systems of partial differential equations. Such a system can be written in general form in an N-dimensional space $X = (x_1, x_2, \ldots, x_{N-1}, t)$ as

$$\frac{\partial U}{\partial t} + \sum_{j=1}^{N-1} \left(C_j \frac{\partial F_j}{\partial x_j} + E_j \right) = 0 \qquad (1)$$

where U and E_j are vectors of dimension M; F_j is a vector of dimension M_j, and C_j is an M x M_j matrix. The coordinate t is the coordinate direction in which the solution is advanced. t can be either a time or space coordinate. U is the solution or state vector of the system. Given the initial conditions at $t = t_o$, we seek to solve for $U(x_1, x_2, \ldots, x_{N-1}, t)$ for $t > t_o$. In general, C_j, F_j, E_j are functions of the space X and the elements of U. Letting I represent the identity matrix and ϕ the null vector (vector whose elements are all zero) we say that Eq. (1) is written in strong conservation form (or divergence law form) if $C_j = I$ and $E_j = \phi$ for all j, or weak conservation form if $C_j = I$ for all j. Otherwise, Eq (1) is said to be in nonconservation form. In the next chapters only solution methods for the equations in conservation form will be discussed.

2.1 Time-Dependent Navier Stokes Equations

The system of time-dependent Navier Stokes equations written in strong conservation form in a Cartesian coordinate system of three spatial dimensions (x, y, z) is

$$\frac{\partial U}{\partial t} + \frac{\partial F_1}{\partial x} + \frac{\partial F_2}{\partial y} + \frac{\partial F_3}{\partial z} = 0 \qquad (2)$$

where N = 4 and

$$U = \begin{Bmatrix} \rho \\ \rho u \\ \rho v \\ \rho w \\ E \end{Bmatrix}, \qquad F_1 = \begin{Bmatrix} \rho u \\ \rho u^2 + \sigma_x \\ \rho uv + \tau_{xy} \\ \rho uw + \tau_{xz} \\ (E+\sigma_x)\, u + \tau_{xy} v + \tau_{xz} w - k \dfrac{\partial T}{\partial x} \end{Bmatrix},$$

$$F_2 = \begin{Bmatrix} \rho v \\ \rho uv + \tau_{xy} \\ \rho v^2 + \sigma_y \\ \rho vw + \tau_{yz} \\ (E+\sigma_y)\, v + \tau_{xy} u + \tau_{yz} w - k \dfrac{\partial T}{\partial y} \end{Bmatrix} \qquad F_3 = \begin{Bmatrix} \rho w \\ \rho uw + \tau_{xz} \\ \rho vw + \tau_{yz} \\ \rho w^2 + \sigma_z \\ (E+\sigma_z)\, w + \tau_{xz} u + \tau_{yz} v - k \cdot \dfrac{\partial T}{\partial z} \end{Bmatrix}$$

The marching coordinate is the time t. The velocities in the coordinate directions x, y, z are represented by u, v, w and the pressure p is obtained from an equation of state as a function of density ρ and specific internal energy e

$$e = \frac{E}{\rho} - \frac{u^2 + v^2 + w^2}{2}$$

where E is the total energy. For an ideal gas, where the ratio of the specific heats γ is a constant, the equation of state is

$$p = (\gamma-1)\ \rho e$$

Other examples for real gases are shown in Ref. 4.

2.2 Time-Dependent Euler Equations

The time-dependent Navier Stokes equations reduce to the Euler equations for inviscid flow if the stress tensor $\overline{T}$ only contains as normal stress the pressure p and if k = 0.

Therefore also Eq. (2) is valid, but now using

$$F_1 = \begin{Bmatrix} \rho u \\ \rho u^2 + p \\ \rho v \\ \rho w \\ (E+p)\ u \end{Bmatrix}, \quad F_2 = \begin{Bmatrix} \rho v \\ \rho uv \\ \rho v^2 + p \\ \rho vw \\ (E+p)\ v \end{Bmatrix}, \quad F_3 = \begin{Bmatrix} \rho w \\ \rho uw \\ \rho vw \\ \rho w^2 + p \\ (E+p)\ w \end{Bmatrix}$$

Again, the equation of state is being used to compute the pressure p.

2.3 Steady Euler Equations for Supersonic Flow

We assume that within the domain for which we seek a solution, the velocity in one coordinate direction is always supersonic. If $u > c$, where c is the local speed of sound (for an ideal gas $C = \sqrt{\gamma \cdot p/\rho}$) we may use the coordinate x as the marching coordinate. The steady Euler equations in a Cartesian coordinate system of three spatial dimensions written in strong conservation form are

$$\frac{\partial U}{\partial x} + \frac{\partial F_1}{\partial y} + \frac{\partial F_2}{\partial z} = 0 \qquad (3)$$

where N = 3 and

$$U = \begin{Bmatrix} \rho u \\ \rho u^2 + p \\ \rho uv \\ \rho uw \\ (E+p)\ u \end{Bmatrix}, \quad F_1 = \begin{Bmatrix} \rho v \\ \rho uv \\ \rho v^2 + p \\ \rho vw \\ (E+p)\ v \end{Bmatrix}, \quad F_2 = \begin{Bmatrix} \rho w \\ \rho uw \\ \rho vw \\ \rho w^2 + p \\ (E+p)\ w \end{Bmatrix}$$

If the flow is uniform at some upstream location $x = x_o$ for all y, z in the domain, the above system can be simplified since total canthalpy $H_T = (E+p)/\rho$ is constant. Thus there is no need to include the energy equation in the above system. The resulting system is

$$\frac{\partial U}{\partial x} + \frac{\partial F_1}{\partial y} + \frac{\partial F_2}{\partial z} = 0 \qquad (4)$$

where now

$$U = \begin{Bmatrix} \rho u \\ \rho u^2 + p \\ \rho uv \\ \rho uw \end{Bmatrix}, \quad F_1 = \begin{Bmatrix} \rho v \\ \rho uv \\ \rho v^2 + p \\ \rho vw \end{Bmatrix}, \quad F_2 = \begin{Bmatrix} \rho w \\ \rho uw \\ \rho vw \\ \rho w^2 + p \end{Bmatrix}$$

and $p = \frac{\gamma-1}{\gamma} \rho \left\{H_T - \frac{u^2+v^2+w^2}{2}\right\}$

2.4 Transformed Equations

It is often convenient for both analytical and/or computational purposes to transform a system of equations into a new coordinate system more natural to the fluid domain or as a consequence of a closen mesh generation. One simple example is the transformation into a cylindrical coordinate system (see, e.g. Kuttar at al in Ref. 5). For more general curvilinear coordinate systems these transformations become very complex. However, as shown by Viviand in Ref. 6, this will not change the conservation properties of the governing equations. Since we will only discuss finite volume methods in the present paper, no coordinate transformation is needed as shown in the following section.

2.5 Finite Volume Approach

The form we now consider is the integral form of a system of hyperbolic equations which can be expressed in conservation form. It is an useful form for both physical and computational purposes. If the hyperbolic system is expressed as

$$\frac{\partial \vec{U}}{\partial t} + \sum_{j=1}^{N-1} \frac{\partial \vec{F}_j}{\partial x_j} = 0$$

then by defining the flux-tensor $\bar{\bar{H}} = \sum_{j=1}^{N-1} \vec{F}_j \, i_j^D$, where $\vec{i}_j$ are unit vectors in the x_j coordinate directions, we can rewrite the system as

$$\frac{\partial \vec{U}}{\partial t} + \nabla \bar{\bar{H}} = 0$$

Integrating this equation within a volume V contained in the domain and enclosed by the surface S yields

$$\frac{\partial}{\partial t} \int_V \vec{U} dv + \int_S \bar{\bar{H}} ds = 0 \qquad (5)$$

for volumes or meshes fixed in time where the direction of $\vec{ds}$ is that of the outer normal to the surface S. For meshes moving in time Eq. (5) has to be written as

$$\frac{\partial}{\partial t}\int_{v(t)} \vec{U}dv + \int_{S(t)} \vec{\vec{H}}d\vec{s} - \int_{S(t)} \vec{U} \cdot \vec{\lambda}\, d\vec{s} = 0 \qquad (6)$$

with $\vec{\lambda}$ as local velocity of ds (mesh velocity).

Eq. (5) and (6) can physically be exposed as the total flux balance in a control volume.

2.6 Relationat at Discontinuities

Following the analysis of Lax [7], a solution to a system of differential equations in a domain is called genuine if it and its first partial derivatives are continuous everywhere in the domain D. A weak solution is also a solution of the system but is genuine only in subdomains of D. The subdomains are separated by surfaces in D across which the solution is allowed to be discontinuous. Relations governing jumps in the values of the dependent variables across discontinuities may be obtained for systems in conservation form by integrating the system about a small volume containing a portion of the surface. For example, a surface of slope tan ϕ in the (x_j, x_α) plane is shown in Fig. 1. For simplicity, the surface is assumed to be orthogonal to all the other coordinate directions. Using the conservation equations from the previous chapter we obtain with the areas of the surfaces S_3 and $S_4 \to 0$:

$$F_{\alpha_1} \vec{i}_\alpha \cdot \vec{n}_{S_1} + F_{j_1} \vec{i}_j \cdot \vec{n}_{S_1} + F_{\alpha_2} \cdot \vec{i}_\alpha \cdot \vec{n}_{S_2} + F_{j_2} \cdot \vec{i}_j \cdot \vec{n}_{S_2} = 0$$

or

$$(F_{\alpha_2} - F_{\alpha_1}) \, (\tan\phi)^{-1} = F_{j_2} - F_{j_1}$$

The above jump relation is commonly known as the Rankine-Hugoniot equation. If $x_\alpha = t$, then $(\tan\phi)^{-1} = U_S$, the speed of the discontinuity (shock wave speed), and the relation determines the jump across a moving discontinuity. If x_α is a spatial coordinate, the relation specifies the jump across a steady oblique discontinuity.

3. NUMERICAL DISCRETISATION

The discretization procedure for Eq. (5) or (6) follows the method of lines in decoupling the approximation of the spatial and time dpendent terms. The computational domain is divided into quadrilateral cells for two-dimensional flows or hexahedrons for three-dimensional flows. For simplicity the spatial discretisation will be discussed on the basis of two-dimensional flows only.

A system of ordinary differential equations is obtained by applying Eq. (5) or (6) to each cell separately. The resulting equations can then be solved by several alternative time stepping schemes. The present paper will only discuss central approximations and Runge-Kutta-type stepping schemes since they proved to be extremely valuable. The most widely used schemes are those of Mac Cormack, e.g. see Ref. 8, or Lax-Wendroff [9]. Detailed descriptions of these schemes are found in the cited literature.

3.1 Central Space Approximations

The physical space is discretised into a mesh of quadrilateral cells as sketched in Fig. 2. Let the values of the quantities associated with each cell be denoted by i,j. In a cell-centered scheme these can be regarded as values at the cell center, or

$$U_{i,j} = \frac{\int\int U \, dvol}{\int\int dvol}$$

For each cell Eq. (5) can be expressed as

$$\frac{d}{dt}(UV) + Q \cdot U = 0 \tag{7}$$

where V is the cell area, and the operator Q represents an approximation to the boundary integral defined by the second integral in Eq. (5). This is defined as follows. Let Δx_k and Δy_k be the movements of x and y along side k of the cell, with appropriate signs. Then the flux balance for, say, the x-momentum component, is represented as

$$\frac{\partial}{\partial t}(\rho V) + \sum_{k=1}^{4} (Q_k \rho u_k + \Delta y_k \cdot p_k) = 0 \tag{8}$$

Where Q_k is the flux velocity

$$Q_k = \Delta y_k U_k - \Delta x_K V_k \tag{9}$$

and the sum is over the four sides of the cell. Each quantity such as U_2 or $(\rho u)_2$ is evaluated as the average of the values in the cells on the two sides of the face,

$$(\rho u)_2 = \frac{1}{2}\{(\rho u)_{i,j} + (\rho u)_{i+1,j})\} \tag{10}$$

for example. The scheme reduces to a central difference scheme on a Cartesian grid, and is second order accurate provided that the mesh function is smooth enough.

A similar nodal point scheme can be constructed as shown in Fig. 3. Now all U are defined in the nodal points i,j, itself and the first integral in Eq. (5) is approximated as

$$\frac{d}{dt}\int_V U dvol = \frac{d}{dt}\{\frac{1}{4}(U_{i,j}+U_{i-1,j}+U_{i,j-1}+U_{i-1,j-1}) \cdot V\}$$

Consequently, the quantities such as U_2, ρU_2 are now evaluated as the averages

$$(\rho U)_2 = \frac{1}{2} \{(\rho U)_{i,j-1} + (\rho U)_{i,j}\}$$

For mesh refinements and multi-grid techniques such nodal point schemes seem to be more appropriate since the quantities U are defined on coinciding points after mesh halfing and interpolation is simplified.

3.2 Dissipative Terms

To suppress the tendency for odd and even point decoupling, and to prevent the appearance of wiggles in regions containing severe pressure gradients in the neighborhood of shock waves or stagnation points, it proves necessary to augment the finite volume scheme by the addition of artificial dissipative terms. Therefore equation (7) is replaced by the equation

$$\frac{d}{dt} (UV) + QU - DU = 0 \qquad (11)$$

where Q is the spatial discretization operator defined by equations (8-10), and D is a dissipative operator. Extensive numerical experiments have established that an effective form for DW is a blend of second and fourth differences with coefficients which depend on the local pressure gradient.

The construction of the dissipative terms for each of the four dependent variables is similar. For the density equation

$$D\rho = D_x\rho + D_y\rho \qquad (12)$$

where $D_x\rho$ and $D_y\rho$ are corresponding contributions for the two coordinate directions, written in conservation form

$$D_x = d_{i+\frac{1}{2},j} - d_{i-\frac{1}{2},j} \tag{13}$$

$$D_y\rho = d_{i,j+\frac{1}{2}} - d_{i,j-\frac{1}{2}}$$

The terms on the right all have a similar form:
for example

$$d_{i+\frac{1}{2},j} = \frac{V_{i+\frac{1}{2},j}}{\Delta t} \begin{matrix} \varepsilon^{(2)}_{i+\frac{1}{2},j} (\rho_{i+1,j} - \rho_{i,j}) \\ -\varepsilon^{(4)}_{i+\frac{1}{2},j} (\rho_{1+2,j} - 3\,\rho_{i+1,j} \\ + 3\,\rho_{i,j} - \rho_{i-1,j}) \end{matrix} \tag{14}$$

where V is the cell volume, and the coefficientes $\varepsilon^{(2)}$ and $\varepsilon^{(4)}$ are adapted to the flow. Define

$$\nu_{i,j} = \frac{|P_{i+1,j} - 2p_{i,j} + p_{i-1,j}|}{|P_{i+1,j}| + 2\,|P_{i,j}| + |P_{i-1,j}|} \tag{15}$$

Then

$$\varepsilon^{(2)}_{i+\frac{1}{2},j} = \kappa^{(2)} \max (\nu_{i+1,j}, \nu_{i,j}) \tag{16}$$

and

$$\varepsilon^{(4)}_{i+\frac{1}{2},j} = \max (0, (\kappa^{(4)} - \varepsilon^{(2)}_{i+\frac{1}{2},j})) \tag{17}$$

where typical values of the constants $\kappa^{(2)}$ and $\kappa^{(4)}$ are

$$\kappa^{(2)} = \frac{1}{4}, \quad \kappa^{(4)} = \frac{1}{256}$$

The dissipative terms for the remaining equations are obtained by substituting ρu, ρv and E for ρ in these formulas.

The scaling $V/\Delta t$ in equation (14) conforms to the inclusion of the cell area V in the dependent variables of equation (10). Since equation (14) contains undivided differences, it follows that if $\varepsilon^{(2)} = O(\Delta x^2)$ and $\varepsilon^{(4)} = O(1)$, then the added terms are of order Δx^3. This will be the case in a region where the flow is smooth. Near a shock wave $\varepsilon^{(2)} = O(1)$, and the scheme behaves locally like a first order accurate scheme.

It has been found that in smooth regions of the flow, the scheme is not sufficiently dissipative unless the fourth differences are included, with the result that calculations will generally not converge to a completely steady state. Instead, after they have reached an almost steady state, oscillations of very low amplitude continue indefinitely (with $\max \frac{\partial \rho}{\partial t} \sim 10^3$, for example).

Near shock waves it has been found that the fourth differences tend to induce overshoots, and therefore they are switched off by subtracting $\varepsilon^{(2)}$ from $\kappa^{(4)}$ in equation (17).

3.3 Time Stepping Schemes

Stable time stepping methods for equation (10) can be patterned on standard schemes for ordinary differential equations. Multistage two level schemes of the Runge Kutta type have the advantage that they do not require any special starting procedure, in contrast to leap frog and Adams Bashforth methods, for example. The extra stages can be used either

(1) to improve accuracy, or
(2) to extend the stability region.

An advantage of this approach is that the properties of these schemes have been widely investigated, and are readily available in textbooks on ordinary differential equations.

Consider a linear system of equations

$$\frac{dU}{dt} + AU = 0.$$

Suppose that A can be expressed as $A = T\Lambda T^{-1}$ where T is the matrix of the eigenvectors of A, and Λ is diagonal. Then setting $v = V^{-1}U$ yields separate equations

$$\frac{d}{dt} v_k + \lambda_k v_k = 0$$

for each dependent variable v_k. The stability region is that region of the complex plane containing values of $\lambda\Delta t$ for which the scheme is stable. Consider now the model problem

$$\frac{\partial u}{\partial t} + a \frac{\partial u}{\partial x} + \varepsilon\Delta x \frac{\partial^2 u}{\partial x^2} = 0 \qquad (18)$$

on a uniform mesh with interval Δx, with a dissipative term of order Δx. This can be reduced to a system of ordinary differential equations by introducing central-difference approximations for $\frac{\partial}{\partial x}$ and $\frac{\partial^2}{\partial x^2}$:

$$\frac{du_i}{dt} + \frac{a}{\Delta x}(u_{i+1} - u_{i-1}) + \frac{\varepsilon}{\Delta x}(u_{i+1} - 2u_i - u_{i-1}) = 0$$

Taking the Fourier transform in space

$$\hat{u} = \frac{1}{2\pi} \int_{-\infty}^{\infty} u e^{i\omega x} dx$$

this becomes

$$\frac{d\hat{u}}{dt} + \lambda\hat{u} = 0$$

where

$$\lambda = \frac{1}{\Delta x} (i\ a \sin \omega\Delta x - 4\varepsilon \sin^2 \frac{\omega\Delta x}{2})$$

It can be seen that the maximum allowable value of the imaginary part of $\lambda\Delta t$ determines the maximum value of the Courant number $a \frac{\Delta t}{\Delta x}$ for which the calculation will be stable, while the addition of the dissipative term shifts the region of interest to the left of the imaginary axis.

In the present case, if the grid is held fixed in time so that the cell area V is constant, the system of equations (10) has the form

$$\frac{dU}{dt} + PU = 0 \tag{19}$$

where if Q is the discretization operator defined in Section 3.1, and D is the dissipative operator defined in Section 3.2, the nonlinear operator P is defined as

$$PU \equiv \frac{1}{V} (QU - DU) \tag{20}$$

The investigation has concentrated on two time stepping schemes. The first is a three stage scheme which is defined as follows. Let a superscript n denote the time level, and let Δt be the time step. Then at time level n set

$$\begin{aligned} W^{(0)} &= U^n \\ U^{(1)} &= U^{(0)} - \Delta t\ PU^{(0)} \\ U^{(2)} &= U^{(0)} - \frac{\Delta t}{2} (PU^{(0)} + PU^{(1)}) \\ U^{(3)} &= U^{(0)} - \frac{\Delta t}{2} (PU^{(0)} + PU^{(2)}) \\ U^{n+1} &= U^{(3)} \end{aligned} \tag{21}$$

Variations of this scheme have been proposed by Gary [11], Stetter [12], and Graves and Johnson [13]. It can be regarded as a Crank Nicolson scheme with a fixed point iteration to determine the solution at time level n+1, and the iterations terminated after the third iteration. It is second order accurate in time, and for the model problem (18) with $\varepsilon = 0$, it is stable when the Courant number

$$\left|\frac{a\Delta t}{\Delta x}\right| \leq 2$$

This bound is not increased by additional iterations. Compared with standard third order Runge Kutta schemas, this scheme gives up third order accuracy in time for a larger bound on the Courant number.

The other scheme which has been extensively investigated is the classical fourth order Runge Kutta scheme, defined as follows. At time level n set

$$\begin{aligned}
W^{(0)} &= U^n \\
U^{(1)} &= U^{(0)} - \frac{\Delta t}{2} PU^{(0)} \\
U^{(2)} &= U^{(0)} - \frac{\Delta t}{2} PU^{(1)} \\
U^{(3)} &= U^{(0)} - \Delta t\, PU^{(2)} \\
U^{(4)} &= U^{(0)} - \frac{\Delta t}{6} (PU^{(0)} + 2PU^{(1)} + 2PU^{(2)} + PU^{(3)}) \\
U^{n+1} &= U^{(4)}
\end{aligned} \qquad (22)$$

This scheme is fourth order accurate in time, and for the model problem (18) with $\varepsilon = 0$, it is stable for Courant numbers

$$\left|\frac{a\Delta t}{\Delta x}\right| \leq 2\sqrt{2}$$

Its stability region, which is displayed on page 176 of Ref. [12], for example, also extends well to the left of the imaginary axis, allowing latitude in the introduction of dissipative terms.

Both schemes have the property that if $PU^n = 0$ then $U^{(1)} = U^{(0)}$, and so on, so that $U^{n+1} = U^n$, and the steady state solution is

$$PU = 0$$

independent of the time step Δt. This allows a variable time step determined by the bound on the local Courant number to be used to accelerate convergence to a steady state without altering the steady state.

The expense of re-evaluating the dissipative terms at every stage of these schemes is substantial. One method of avoiding this is to introduce the dissipative terms in a separate fractional step after the last stage of the Runge Kutta scheme. Then equation (20) is replaced by

$$PU \equiv \frac{1}{V} QU \qquad (20)$$

and the fourth order Runge Kutta scheme defined by equation (22), for example, is modified by setting

$$U^{n+1} = U^{(4)} + \frac{\Delta t}{V} DU^{(4)}$$

This method has the advantage that the stability properties for the two fractional steps are independent, so that the scheme will be stable if each fractional step is stable. It has the disadvantage that the steady state solution is no longer independent of the time step.

An alternative approach which has proved successful in practice, is to freeze the dissipative terms at their values in the first stage. Thus the fourth order Runge Kutta scheme is modified so that it has the form

$$
\begin{aligned}
U^{(0)} &= U^{n} \\
U^{(1)} &= U^{(0)} - \frac{\Delta t}{2V} QU^{(0)} + \frac{\Delta t}{2V} DU^{(0)} \\
U^{(2)} &= U^{(0)} = \frac{\Delta t}{2V} QU^{(1)} + \frac{\Delta t}{2V} DU^{(0)} \\
U^{(3)} &= U^{(0)} = \frac{\Delta t}{2V} QU^{(2)} + \frac{\Delta t}{V} DU^{(0)} \\
U^{(4)} &= U^{(0)} - \frac{\Delta t}{6V} (QU^{(0)} + 2QU^{(1)} + 2QU^{(2)} + QU^{(3)}) + \frac{\Delta t}{V} DU^{(0)}
\end{aligned}
\tag{23}
$$

The operators Q and D require roughly equal amounts of computation. Assigning to each 1 unit of work, and assuming that dissipative terms would be required in the leap frog or Mac Cormack schemes, both of which have maximum time steps bounded by a Courant number of one, one obtains the following table for the relative efficiency of the schemes:

Scheme	Evaluations of QU	Evaluations of DU	Work	Maximum Courant Number	Efficiency = $\frac{\text{time step}}{\text{work}}$
Leap frog	1	1	2	1	1/2
MacCormack	2	1	3	1	1/3
3 stage	3	3	6	2	1/3
4 stage	4	4	8	2.8	.35
4 stage (frozen DU)	4	1	5	2.8	.56

3.4 Boundary Conditions

Improper treatment of the boundary conditions can lead to serious errors and perhaps instability. In order to treat the flow exterior to a profile one must introduce an artificial outer boundary to produce a bounded domain. If the flow is subsonic at infinity there will be three incoming characteristics where there is inflow across the boundary, and one outgoing characteristic, corresponding to the possibility of escaping acoustic waves. Where there is outflow,

on the other hand, there will be three outgoing characteristics and one incoming characteristic. According to the theory of Kreiss [14], three conditions may therefore be specified at inflow, and one at outflow, while the remaining conditions are determined by the solution of the differential equation. It is not correct to specify free stream conditions at the outer boundary.

For the formulation of the boundary conditions it is convenient to assume a local transformation to coordinates X and Y such that the boundary coincides with a line Y = constant. Using subscripts X and Y to denote derivatives, the Jacobian

$$h = x_X y_Y - x_Y y_X \tag{24}$$

corresponds to the cell area of the finite volume scheme. Introduce the transformed flux vectors

$$G_1 = y_Y F_1 x_Y F_2, \qquad G_2 = x_X F_2 - y_X F_1 \tag{25}$$

where F_1 and F_2 are defined by equation (2). In differential form equation (2) then becomes

$$\frac{\partial}{\partial t}(hU) + \frac{\partial G_1}{\partial X} + \frac{\partial G_2}{\partial Y} = 0 \tag{26}$$

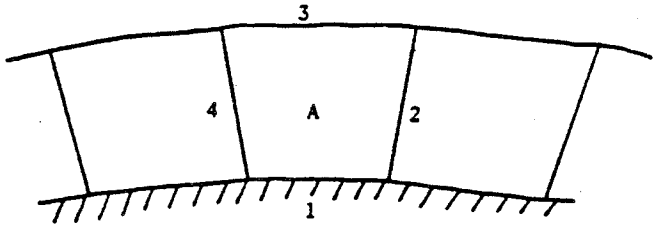

Consider first the boundary condition at the solid wall. Across side 1 of cell A in the sketch there is no convected flux since

$$x_X v - y_X u = 0 \tag{27}$$

But there are contributions Δyp and Δxp to the momentum equations, which require an estimate of the pressure at the wall. Taking the time derivative of equation (27) multiplied by ρ, and substituting for $\frac{\partial}{\partial t}(h\rho u)$ and $\frac{\partial}{\partial t}(h\rho v)$ from equation (26) leads to the relation given by Rizzi in Ref. 13

$$(x_X^2+y_X^2)\, p_y = (x_X x_Y+y_X y_Y)\, p_X + \rho\, (y_Y u-x_Y v)(vx_{XX}+uy_{XX}) \tag{28}$$

Thus we can estimate p_y in terms of quantities which can be determined from the interior solution, and we can use this value of p_y to extrapolate the pressure from the adjacent cell center to the wall. This approach is also called "normal momentum in method". Further techniques are described in Ref. 15 by MacCormack. For fine meshes, the simple $p_x = p_1$ approach proved to be accurate enough for engineering purposes.

Stable boundary conditions have been given by Gottlieb and Turkel (16) and Gustafsson and Oliger (17) for a variety of difference schemes. The treatment of the outer boundary condition adopted here follows similar lines. The equations are linearized about values at the end of the previous time step, and the characteristic variables corresponding to outgoing characteristics are then determined by extrapolation from the interior, while the remaining boundary conditions are specified in a manner consistent with the conditions imposed by the free stream. Let

$$A = \frac{\partial G_1}{\partial U}\,, \quad B = \frac{\partial G_2}{\partial U}$$

Since the boundary is a line Y = constant, the eigenvalues of B determine the incoming and outgoing characteristics. If q_n and q_t are the velocity components normal and tangential to the boundary, and c is the speed of sound, these eigenvalues are q_n, q_t, q_n-c, and q_n+c. Let values at the end of the previous time step be denoted by the subscript o, and let T_o be the eigenvector matrix of B_o. Then B_o is reduced to diagonal form by the transformation $\Lambda_o = T_o^{-1} B_o T_o$, and setting $v = T_o^{-1} U$ the linearized equation assumes the form

$$\frac{\partial}{\partial t}(hv) + T_o^{-1} A_o T_o \frac{\partial v}{\partial X} + \Lambda_o \frac{\partial v}{\partial y} = 0$$

The characteristic variables are the components of v. These are $p-c_o^2\rho$, q_t, $p-\rho_o c_o q_n$ and $p_o+\rho_o c_o q_n$.

Let values extrapolated from the interior and free stream values be denoted by the subscripts e and ∞. Then at the inflow boundary we set

$$p - c_o^2\rho = p_\infty - c_o^2\rho_\infty \tag{29a}$$

$$q_t = q_{t_\infty} \tag{29b}$$

$$p - \rho_o c_o q_n = p_\infty - \rho_o c_o q_{n_\infty} \tag{29c}$$

$$p + \rho_o c_o q_n = p_e + \rho_o c_o q_{n_e} \tag{29d}$$

yielding

$$p = \frac{1}{2}\left(p_e + p_\infty + \rho_o c_o \left(q_{n_e} - q_{n_\infty}\right)\right)$$

$$q_n = q_{n_\infty} + \frac{p-p_\infty}{\rho_o c_o}$$

The density can be determined from (28a). For steady state calculations it can alternatively be determined by specifying that the total enthalpy H has its free stream value.

At the outflow boundary one condition should be specified. If the flow is a parallel stream then $\frac{\partial p}{\partial y} = 0$, so for an open domain

$$p = p_\infty \tag{30}$$

A non reflecting boundary condition which would eliminate incoming waves is

$$\frac{\partial}{\partial t}(p-\rho_o c_o q_n) = 0 \tag{31}$$

This does not assure (30). Following Rudy and Strikwerda (18), (30) and (31) are therefore combined as

$$\frac{\partial}{\partial t}(p-\rho_o c_o q_n) + \alpha(p-p_\infty) = 0 \tag{32}$$

where a typical value of the parameter α is 1/8. The velocity components and energy are extrapolated from the interior.

Various other boundary conditions designed to reduce reflections from the outer boundary have been proposed by several authors (19.20), and it seems that it would be worth while to test some of these alternatives.

A very simple set of quite efficient boundary conditions can be found by using the flux variables plus the characteristics to decide upon the number of conditions to be specified. For flows entering the fluid domain at a boundary only one variable can be extrapolated from inside, e.g. density. If total enthalpy, flow direction, and total pressure are prescribed at the boundary, ρu, ρv, and p can be computed. For flows having the fluid domain a set of exit conditions is derived by prescribing only static pressure p, extrapolating ρu, ρv, E, and computing ρ from the energy equation.

For turbomachinery cascades only periodicity-conditions have to be applied rather than the external far field conditions.

For cases with detached bow shocks it can be desirable to use a moving mesh aligned with the bow shock for better accuracy. All the relations discussed in the previous chapter apply also for such cases if Eq. (6) is discritised. Only the mesh velocity based on the moving, bow shock is required as additional information. Basically, two solution processes are of practical use:

- characteristic relations; for details see Ref. 22 and 23 for two-dimensional flows and Ref. 24 for three space dimensions
- extrapolation of the pressure from inside the domain to the rearward facing side of the shock and application of the classical shock relations as discussed in section 2.6.

Comparisons of both approaches in Ref. 25 indicate that the second approach especially in three space dimensions is superior due to its much easier and faster coding for nearly the same accuracy.

3.5 Kutta Conditions for Lifting Flows

In potential flow theory, Kutta conditions are needed at all surfaces where the flow is leaving the contour, e.g. at trailing edges, side edges. In two-dimensional lifting airfoil flow the classical Kutta-condition says that the static pressure at the trailing edge on upper and lower surface is equal thus the velocity vector is equal in magnitude and direction since in isentropic flow total pressure is constant. This leads to zero velocity at the trailing edge for nonsero trailing edge angle. For three-dimensional lifting flow Mangler and Smith in Ref. 26 discuss in detail possible solutions and trailing edge wakes behind wings. All standard methods in linear and nonlinear compressible potential flow theory assume the wake, and thus the lines with the jump in potential, to leave in the bisector-direction and to have constant jumps in potential along x in spanwise constant locations. The flow around the wing tip in general is neglected. This can cause at higher lift coefficients quite large deviations from the physically correct situation.

Solutions to the full compressible Euler equations do not need any explicit Kutta-condition to be unique, neither in two- or in three-dimensional flow. This might be explained on the basis of Fig. 3. Potential flow needs for uniqueness a Kutta condition, since all rear stagnation point locations are possible. As sketched in Fig. 3a, for all points $q = 0$ and static pressure p = stagnation pressure is a solution. So this point has to be specified by an additional condition.

In the full compressible inviscid equations of motion (Euler) a flow around a sharp corner or an edge with a small radius of curvature will always cause expansion to supersonic flow. As indicated in Fig. 3b, compression to the point where the flow is leaving the surface can only happen through a shock which will cause total pressure loss and a large amount of vorticity due to the combination of shock strength and curvature. This will require a point on the surface with dif-

ferent total pressure which implies different velocities for the same static pressure, i.e. a contact discontinuity or wake like shown in Fig. 3b. However, this solution is not stable since there exists in subsonic flow a solution without any total pressure loss, namely the one with the flow leaving the trailing edge and thus not having the large expansion and the shock. In transonic lifting cases with shocks, the total pressure loss on one side is larger than on the other which will only allow the flow to stagnate at the trailing edge upper surface while the velocity at the trailing edge lower surface is finite, thus leaving the lower surface smoothly as shown in Fig. 3c. The wake contact discontinuity in velocity and total pressure is captured in the fully conservative finite volume scheme. Therefore the wake shape is not fixed due to the mesh but will be a result independent of the mesh chosen.

The same mechanism applies to sharp leading or side edges or when the radius of curvature is small combined with locally supersonic flow.

4. CONVERGENCE ACCELERATION

Different devices can be used to accelerate the convergence of the solution to a steady state. The ones mainly used are implicit approximate factorization techniques which are described in detail in the present short course lecture by R.M. Beam [27]. Those techniques presented here have all in common that they preserve the high degree of vectorization which is possible for explicit schemes on present day or future vector computers.

The first is to use the largest possible time step permitted by the local stability bound everywhere in the computational domain. This has the effect of assuring that disturbances are propogated the whole way across the domain in a number of time steps of the same order as the number of mesh intervals. It can be regarded as scaling the wave speed to give equations of the form

$$\frac{\partial U}{\partial t} + \lambda \left(\frac{\partial F_1}{\partial x} + \frac{\partial F_2}{\partial y}\right) = 0$$

where λ is proportional to the local mesh size. Assuming that a stretched grid is used to the computational domain away from the profile will be very large near the outer edge of the domain.

As a model for this procedure consider the wave equation in polar coordinates r and θ,

$$\phi_{tt} = c^2 \left(\frac{1}{r}\frac{\partial}{\partial r}(r\phi_r) + \frac{1}{r^2}\phi_{\theta\theta}\right)$$

Suppose that the wave speed c is proportional to the radius, say $c = \alpha r$. Then

$$\phi_{tt} = \alpha^2 \left(r\frac{\partial}{\partial r}(r\phi_r) + \phi_{\theta\theta}\right)$$

This has solutions of the form

$$\phi = \frac{1}{r^n} e^{-\alpha n t}$$

suggesting the possibility of exponential decay.

A more sophisticated modification of the equations, which is presently being investigated is to set

$$\frac{\partial U}{\partial t} + M \left(\frac{\partial F_1}{\partial x} + \frac{\partial F_2}{\partial y}\right) = 0$$

where the matrix M couples the equations for ρu, ρv and E, and modifies the eigenvalues of the system. The new MacCormack method [28] verifies this by stripping off the sign of the eigenvalues of the system by using the diagonalisation matrix. An other idea proposed by Jameson is to shift the spectrum of the eigenvalues by adding resp. subtracting the maximum absolut value of eigenvalues. Both techniques lead to block bi-diagonal matrics which can be solved easily.

The second device for convergence acceleration is to introduce a forcing term proportional to the difference between the total enthalpy H and the free stream value H_∞ throughout the domain. The density and energy equations

$$\frac{\partial}{\partial x} (\rho u) + \frac{\partial}{\partial y} (\rho v) = 0$$

and

$$\frac{\partial}{\partial x} (\rho u H) + \frac{\partial}{\partial y} (\rho v H) = 0$$

are then consistent. This property is not preserved by various predictor corrector difference schemes, such as the MacCormack

scheme. It is preserved by the schemes defined in sections above however, provided that the dissipative operator is applied to ρH and not ρE in the energy equation. Thus a forcing term proportional to $H-H_\infty$ does alter the steady state.

The reason for introducing such a term is to provide additonal damping. The term is intended to have an effect similar to that of the term containing ϕ_t in the telegraph equation:

$$\phi_{tt} + \alpha\phi_t = \phi_{xx} + \phi_{yy}$$

Multiplying this equation by ϕ_t, and integrating by parts over all space leads to the relation

$$\frac{\partial P}{\partial t} + \alpha \int_{-\infty}^{\infty}\int_{-\infty}^{\infty} \phi_t^2 \, dxdy = 0$$

where

$$P = \frac{1}{2}\int_{-\infty}^{\infty}\int_{-\infty}^{\infty} (\phi_t^2 + \phi_x^2 + \phi_y^2) \, dxdy$$

Since P is non negative, it must decay if $\alpha > 0$ until $\phi = 0$. When relaxation methods are regarded as simulating time dependent equations, it is similarly found that the term containing ϕ_t plays a critical role in determining the rate of convergence [29].

In subsonic flow the Euler equations are equivalent to the unsteady potential flow equation

$$\phi_{tt} + 2u\phi_{xt} + 2v\phi_{yt} = (c^2-u^2)\,\phi_{xx} - 2uv\phi_{xy} + (c^2-v^2)\,\phi_{yy} \qquad (33)$$

which can be reduced to the wave equation by introducing moving coordinates $x^1=x-ut$, $y^1=y-vt$. Also the unsteady Bernoulli equation is

$$\phi_t + H = H_\infty$$

It can be verified that if the Euler equations are written in primitive form, and the density equation is modified by the addition of a term proportional to $H-H_\infty$, so that it becomes

$$\frac{\partial \rho}{\partial t} + u \frac{\partial \rho}{\partial x} + v \frac{\partial \rho}{\partial y} + \rho \left(\frac{\partial u}{\partial x} + \frac{\partial v}{\partial y}\right) + \alpha \rho \left(H-H_\infty\right) = 0$$

then the flow remains irrotational in the absence of shock waves, and equation (33) is modified by a term proportional to ϕ_t. When the density equation is combined with the momentum equations to yield a system of equations in conservation form, the modified equations become

$$\frac{\partial \rho}{\partial t} + \frac{\partial}{\partial x}(\rho u) + \frac{\partial}{\partial y}(\rho v) + \alpha \rho \left(H-H_\infty\right) = 0$$

$$\frac{\partial}{\partial t}(\rho u) + \frac{\partial}{\partial x}(\rho u^2+p) + \frac{\partial}{\partial y}(\rho v u) + \alpha \rho u \left(H-H_\infty\right) = 0$$

$$\frac{\partial}{\partial t}(\rho v) + \frac{\partial}{\partial x}(\rho u v) + \frac{\partial}{\partial y}(\rho v^2+p) + \alpha \rho v \left(H-H_\infty\right) = 0$$

$$\frac{\partial}{\partial t}(E) + \frac{\partial}{\partial x}(\rho u H) + \frac{\partial}{\partial y}(\rho v H) + \alpha \rho H \left(H-H_\infty\right) = 0$$

The energy equation now has a quadratic term in H, like a Riccati equation. This can be destabilizing, and an alternative which has been found effective in practice is to modify the energy equation to the form

$$\frac{\partial}{\partial t}(E) + \frac{\partial}{\partial x}(\rho u H) + \frac{\partial}{\partial y}(\rho v H) + \alpha \left(H-H_\infty\right) = 0$$

which tends to drive H towards H_∞. The added terms can conveniently be introduced in a separate fractional step at the end of each time step.

The third device for convergence acceleration is the multiple grid technique which has been demonstrated to be a very powerful for quasi-linear second order differential equations by South and Brandt [30] as well as Jameson [31]. However, techniques being developed for the full potential equation cannot be simply applied for the Euler or Navier Stokes equations. Brandt [32] proposed a multi-grid solver for the steady Euler and Navier Stokes equations, while Ni [33] presented a multiple grid technique based on a one step distribution formula scheme for the Euler equations. We tried the multiple grid technique in combination with the center point as well as the nodal point Runge Kutta time stepping and with a Ni-type one step scheme. In general nodal point schemes are better suited to multi-grid techniques since after each mesh halving mesh points will remain mesh points in the coarser mesh. Best results so far have been obtained using the one step distribution formula scheme of Ni. Therefore this procedure is described briefly. For details we refer to Ref. 33.

The basic idea is to use the coarser grids to propagate the fine grid corrections properly and rapidly through out the field, thus improving convergence rate to steady state while maintaining low truncation errors by using the fine grid discretisation.

The changes ΔU_{2h} in the coarse grid, obtained by removing every other line from the fine grid, are determined by

$$\Delta U_{2h} = I_{2h}^{h} \, \delta U_{h} \tag{34}$$

Where I_{2h}^{h} is operator which transfers to each control volume of the coarse grid the correction δU_{H} of the fine grid using specific distribution formulas.

After computing the corrections δU_{2h} on all coarse grid points the flow properties at the finest grid are updated by

$$U^h = U + I_h^{2h} \delta U_{2h} \tag{35}$$

where I_h^{2h} is a linear interpolation operator which interpolates the coarse grid corrections to give the connections at each fine grid point of the finest mesh.

The scheme is quite sensitive to the choice of distribution formulas and the boundary condition treatment. Also, compared with the Runge-Kutta stepping schemes, a fairly large dissipation has to be incorporated to make multi-grid converging efficiently.

5. MODEL-EXAMPLE BURGERS EQUATION

To gain better insight into the numerical behaviour of the Runge Kutta stepping schemes with central differences, the three-stage scheme has been applied to the inviscid Burgers equation in divergence form

$$\frac{\partial U}{\partial t} + \frac{\partial F}{\partial x} = 0, \quad F = \frac{1}{2} U^2 \tag{36}$$

Following Eq. (21) we get

$$\begin{aligned}
U^{(0)} &= U^n \\
U^{(1)} &= U^{(0)} - \frac{\Delta t}{\Delta x} \left(F^{(0)}_{i+1/2} - F^{(0)}_{i-1/2}\right) \\
U^{(2)} &= \frac{1}{2} \left\{U^{(1)} + U^{(1)} - \frac{\Delta t}{\Delta x} \left(F^{(1)}_{i+1/2} - F^{(1)}_{i-1/2}\right)\right\} \\
U^{(3)} &= \frac{1}{2} \left\{U^{(0)} + U^{(1)} - \frac{\Delta t}{\Delta x} \left(F^{(2)}_{i+1/2} - F^{(2)}_{i+1/2}\right)\right\} \\
U^{h+1} &= U^{(3)}
\end{aligned} \tag{37}$$

where $F^{(0)}$ is being evaluated from $U^{(0)}$, $F^{(1)}$ from $U^{(1)}$, etc. $F_{i+1/2}$ is being approximated by

$$F_{i+1/2} = F \left\{\frac{1}{2} \left(U_i + U_{i+1}\right)\right\}$$

One example of including the mentioned second order filter is to add one filter step after the Runge Kutta stepping, e.g.

$$U^{h+1} = U^{(3)} + \frac{\Delta t}{\Delta x} \delta^- \left\{\mu \left(\delta^+ U^{(3)}\right)\right\} \tag{38}$$

with δ^- as backward and δ^+ as forward differences operator

$$\delta^+ U_i = U_{i+1} - U_i \text{ etc.}$$

The coefficient μ is given by

$$\mu = \frac{\left| U_{i+1}^{(3)} - 2\, U_i^{(3)} + U_{i-1}^{(3)} \right|}{\left| U_{i+1}^{(3)} \right| + 2 \left| U_i^{(3)} \right| + \left| U_{i-1}^{(3)} \right|}$$

In Ref. 34 a large variety of computations have been carried out using different initial conditions and different filter schemes. Only two cases will be discussed here; for people interested, a program listing has been added at the end. Fig. 4 shows the results for the fan solution without any filter step in comparison with the exact solution. The agreement is quite good. The result in Fig. 5a for the shock jump solution without any filtering shows quite large oszillations around the discontinuity after the dimensionles time t = 2.25. However, they can be damped nicely by using the additional filter step as indicated in Fig. 5b.

6. MESH GENERATION

The presented numerical schemes allow in principle the computation of complete three-dimensional aircraft flow fields, however the geometry discretisation along with the mesh generation is limiting presently the complexity. Mesh generation is a difficult and rather lengthy problem and will not be discussed here in detail. Ref. 35-39 give an overview over the present state. We will only mention the basic mesh topologies which have been used in connection with the Runge-Kutta Stepping schemes.

In two-dimensional airfoil flow parabolic C-type meshes are easily established with good resolution near the leading edge and lines which can be aligned with the wake. These meshes can easily be extended to treat airfoils between walls or turbomachinery cascades as shown in Fig. 6. However, the best trailing edge resolution can be obtained by using an O mesh as known from conformal mapping. This mesh also maximises the number of points on the surface for a given total amount. Fig. 7 represents a typical example. For two-dimensional or axisymmetric inlets very efficient mesh systems can be generated by using Maxwell-transformations [40] as shown on Fig. 8.

Three-dimensional wings and wing-body combinations are treated by either C-H or O-H type meshes being generated either by solving a Poisson equation [35] or using transfinite interpolation [38]. Fig. 9 shows two examples. Three-dimensional inlets or body-mounted inlets can be discretised by using the previously mentioned 2-D mesh projected on the body and used for each inlet section as shown in Fig. 10. More complex configurations require grid structures as proposed by Lee [37]. We are presently pursuing such block structured meshes for complex fighter configurations.

7. RESULTS

Up to now a large number of two- and three-dimensional computations have been performed. Some typical results are shown to demonstrate the accuracy and convergence of the basic numerical algorithm as well as results to show the wide range of possible applications.

7.1 Nonlifting Two-Dimensional Flows

Fig. 11 shows results for the flow past a circular cylinder using the grid of Fig. 7. For Mach numbers 0.20 and 0.35 the flow is fully subsonic and there is no departure from for and aft symmetry as in an exact solution. Indeed, the comparison for M = 0,20 with the full potential solution shows no difference. The calculations are normalised with p = 1, ρ = 1 at infinity, so the quantity S can be used as a measure of entropy generation. The largest computed value of S for M = 0,35 was S = 0,0003, at a point along the surface. At Mach 0,45 there appeared a moderately strong shock wave, as can be seen in Fig. 12. Here entropy was computed to be 0,012 behind the wave. Fig. 12 also includes the convergence history for this case. The measure of convergence is the residual for the density defined as the root mean square value of $\frac{\partial \rho}{\partial t}$ (calculated as $\Delta\rho/\Delta t$ for a complete time step). This was reduced from 1.67 to 0.486 $\cdot$ 10^{-9}. Enthalpy damping was used in this calculation to accelerate convergence. The calculation was started impulsively by suddenly introducing the cylindrical obstacle into the uniform flow, and immediately enforcing the solid wall boundary condition at its surface. This created very large disturbances, but the pattern of the flow field is still quite rapidly established. A measure of this is the size of the supersonic region. In this case the number of supersonic

points was frozen after 450 cycles. Fig. 13 presents similar results for M = 0,50, again in comparison with the full potential results. The additional velocity vector, streamline and isobar-plots clarify the differences between the two solutions. Since the full potential solution has no total pressure loss, the flow at the rear stagnation point has the same cp as the front one. The Euler solution nicely shows the total pressure loss due to the strong shock which leads to the lower rear stagnation point pressure. The largest difference, however, emenates from the separated recirculating flow which is being caused by the vorticity production due to the curved shock and which is then concentrated to a separated region due to the curved streamlines. This separation is to understood as the limit of Reynolds-number to infinity. It is not specific to the present method and was verified by a lot of other methods, e.g. Ref. [41].

Fig. 14 shows results for the flow past a NACA 0012 airfoil using the 65 x 33 O - mesh shown in Fig. 7. Comparing the full potential and the Euler results for M = 0.85, $\alpha = 0^{\circ}$, it can be seen that the shock wave is further aft in the potential flow calculation, which was performed by the fully conservative finite volume method of Jameson and Caughey [2] , using a first order accurate formulation in the supersonic zone. The convergence history of the Euler calculation is also shown in Fig. 14. Fig. 15 presents a similar comparison between the potential flow and Euler results for the NACA 0012 airfoil at M = 0.80. In this case the shock locations are nearly identical, however the jump is sharper in the Euler solution. Also shown are the convergence histories with and without the enthalpy damping. Without enthalpy damping the final residual is $0.269 \cdot 10^{-6}$, with damping it is $0.240 \cdot 10^{-9}$. These runs used the potential flow result as the starting condition for the Euler calculation. Thus the flow pattern was already essentially established at the start of the Euler calculation, with the result that the number of points in the supersonic zone was frozen after 180 cycles when enthalpy damping was used. To illustrate the development of the flow field without the assistence of the potential flow calculation, Fig. 16 shows the results for the same flow after 200, 400, 600, and 800 cycles with an impulsive start.

Fig. 17 presents results for the Euler solution in the same O-mesh at supersonic free stream Mach number = 1.20, $\alpha = 0^{o}$. The captured detached bow shock as well as the oblique shock at the trailing edge can nicely be identified in the JSO-Mach-lines and isobars-plot. The streamline and velocity-vector plots show the flow direction change through the oblique shock.

These results support the conclusions that shock waves can be satisfactorily captured without resorting to flux vector splitting and one sided differencing Ref. 43 - 46 , at least for steady state calculations.

7.2 Two-Dimensional Lifting Flows

Examples using the present schemes in lifting two-dimensional flows have been obtained for inviscid flows and viscid flow using an interaction scheme with the boundary layer. Fig. 18 presents comparisons for the full potential solution using again the scheme described in Ref. 2 and the Euler solver described above for M = 0,80 and $\alpha = 0,37$. Shock positions at upper and lower surface are quite different and the lift coefficient in the Euler solution is only half that one from the full potential solution. Fig. 19 shows results for M = 0,20, $\alpha = 25^{o}$. The flow around the leading edge accelerates to supersonic speed and the potential flow solution clearly shows a shock. The Euler solution, however is quite different behind the supersonic region. The pressure distribution is influenced by the vorticity and total pressure loss being produced and almost tends to separate. A further increase in angle of attack would cause similar results as for the cylinder in Fig. 13. The additional streamline-plot nicely shows that the flow is leaving the lower surface smoothly at the trailing edge. Fig. 20 - 22 show viscid results using the interaction method described in Ref. 47. The comparison with the measurements is quite good. It is also worthwile to note that even the inviscid Euler solution is much closer to the experimental data compared with full potential methods.

On Fig. 23 results are portrayed of Euler-solutions for transonic flow over the Do - A2 (CAST 10-2) airfoil at M = 0.76, $\alpha = 0.5^{o}$ with and without condensation. These results as well as the mathematical treatment of real gas and condensation within the Euler equations have been discussed in Ref. 48 and 49.

By using the mesh shown in Fig. 6 and corresponding periodicity boundary condition, transonic turbomachinery cascades have been analysed in Ref. 50. One of those examples is presented in Fig. 24. Compared with different full potential solvers, again differences occur which now mainly are contributed to the total pressure loss which will cause different flow conditions since only total enthalpy, total pressure, entrance flow angle and exit static pressure plus sidewall contraction ratio have been specified in the Euler computation.

7.3 Three-Dimensional Inlet Flowfields

The three-dimensional Runge Kutte Time Stepping Scheme has been extensively used for transonic and supersonic three-dimensional inelt analysis. A variety of results will be published at the 1982 ICAS Congress in Seattle [51] . For the mesh shown on Fig. 8 the computational results are shown in Fig. 25. The results converged after 300 cycles and the reduction per cycle has been 0.975 for the density time-derivative. As example for supersonic flow with a moving mesh Fig. 26 presents the comparison of the Euler solution with experimental data for a F16-type pitot-inlet, discussed in Ref. 25.

7.4 Three-Dimensional Lifting Wing-Body Combinations

Three-dimensional wing-body combinations have been analysed using the discussed Euler schemes in Ref. 38 and Ref. 47 using the O-O-type mesh of Eriksson or the Yu-type C-H mesh. Detailed comparisons of the four stage Runge Kutte stepping scheme and the full potential solver based on Ref. 2 for the Onera M6 wing and the DFVLR-F4 transport-configuration clearly prove the advantage of the Euler equation solution not needing any Kutta condition. The O-type mesh in spanwise direction provides the accurate modelling of the wing tip even with vortex flow as discussed in the next chapter.

Fig. 27 - 30 show some results from Ref. 38 and 47. The results in Fig. 30 have been performed for both, the full potential and Euler solution on the same mesh.

7.5 Leading Edge Vortex Flows

Separation does not have to be a viscid phenomenon, it can also occur in inviscid flow as shown on Fig. 13 and discussed earlier. Since no Kutta condition is needed at trailing edges in two- and three-dimensional flows, we might argue if separation at leading edges of highly swept wings can be predicted as solution of the compressible Euler equations. If we analyse the wing-body combination of Ref. 52 at $M = 0.40$ and $\alpha = 16^{\circ}$ we obtain supersonic flow at the nose with a shock. The corresponding Euler solution predicts separation and thus the leading edge vortex flow pattern right behind this region. Fig. 31 shows first results. More detailed comparisons will be given in Ref. 53. Fig. 32 shows similar results for a sharp leading edge computed with the three-stage scheme and the second order filter $\varepsilon^{(4)}$ only. These results are discussed further in Ref. 54, however the peak at the leading edge in pressure seems to be questionable.

8. CONCLUSIONS

The objectives of the present short course contribution were to present an efficient and accurate solver to the full compressible Euler equations to compute transonic and supersonic flow over two- and three-dimensional configurations. Since in demonstration cases the same meshes were used in the Euler solver as in the full potential solver, the main differences in solutions of the fully conservative full potential equation and the Euler equations could be demonstrated. The most important information has been that Euler solvers do not need any explicit Kutta condition to be unique. Even on smooth surfaces separation can occur in inviscid compressible flow caused by total pressure loss and vorticity due to a shock. These effects help explaining the a apriori unexpected difference between lifting Euler and full potential solutions. For viscous flows the Euler equations solver have been successfully coupled with an inverse boundary layer method. The same solver, however, can also be applied to the time-averaged Navier Stokes equations. To further improve the computational efficiency, the acceleration techniques multi-grid and implicit filtering as discussed in Section 4 are presently under further development.

Attractive features of the presented Runge Kutta Schemes are their comparative simplicity, and their susceptibility to the extensive use of vector operations on a vector computer. The present implementation of the fourth oder Runge Kutta Scheme requires in two-dimensional flow about 400 floating point operations at each interior cell. In tests on a CRAY 1 computer a computing speed of almost 100 megaflops per second have been obtained. All codes are written in standard Fortran, and this rate was achieved simply by relying on the capability of the CRAY Fortran compiler to vectorize the code automatically. A still higher rate could be realized by writing certain critical segments of the program in assembly language. In practice a typical run is sufficiently converged in a fine mesh within 300 to 500 cycles for engineering applications. This can be further improved by using mesh-refinement.

9. ACKNOWLEDGEMENTS

We would like to thank our colleages Prof. Whitfield, Dr. Rizzi, Dr. Grashof, Dr. Haase, Dr. Wagner and Mr. Leicher for participating in the development and evaluation of the methods for different studies and providing results.

10. REFERENCES

[1] Ballhaus, W.F.
Some Recent Progress in Transonic Flow Computations.
VKI-LS87, March 1976, Brüssel

[2] Caughey, D. and Jameson, A.
Basic Advances in the Finite Volume Method for Transonic Potential Flow Calculations. Symposium on Numerical and Physical Aspects of Aerodynamic Flows, Long Beach, 1981

[3] Schmidt, W.
Aerodynamic Subsonic/Transonic Aircraft Design Studies by Numerical Methods. AGARD-CP-285, Paper 9, 1980

[4] MacCormack, R.W. and Warming, R.F.
Survey of Computational Methods for Three-Dimensional Supersonic Inviscid Flows with Shocks.
AGARD-LS-64, Paper 5, 19, 1973

[5] Kutler, P., Rainhardt, W.A., and Worming, R.F.:
Numerical Computation of Multishocked, Three-Dimensional Supersonic Flow Fields with Real Gas Effects. AIAA Paper 72-702, 1972

[6] Viviand, H.
Formes Conservatives des equations de la dynamique des gaz. La Rech. Aerosp. No. 1971-1, 1974, pp 65-66

[7] Lax, P.D.
Weak Solutions of Nonlinear Hyperbolic Equations and Their Numerical Computation. Comm. Pure and Appl. Math., Vol. 7, 1954

[8] MacCormack, R.W.
The Effect of Viscosity in Hypervelocity Impact Cratering. AIAA Paper 69-354, 1969

[9] Lax, P.D. and Wendroff, B.
Difference Schemes for Hyperbolic Equations with High Order of Accuracy. Comm. Pure and Appl. Math., Vol. 17, 1964

[10] Viviand, H.
Pseudo Unsteady Methods for Transonic Flow Computations. Proceedings of Seventh International Conference on Numerical Methods in Fluid Dynamics, Stanford, 1980, Springer-Verlag, 1981

[11] Gary, J.
On Certain Finite Difference Schemes for Hyperbolic Systems. Math. Comp., Vol. 18, pp. 1-18, 1964.

[12] Stetter, H.J.
Improved Absolute Stability of Predictor-Corrector Schemes, Computing, Vol. 3, pp. 286-296, 1968

[13] Graves, R. and Johnson, N.
Navier Stokes Solutions Using Stetter's Method. AIAA Journal, Vol. 16, pp. 1013-1015, 1978

[14] Kreiss, H.O.
Initial Boundary Value Problems for Hyperbolic Systems. Comm. Pure Appl. Math., Vol. 23, pp. 277-298, 1970

[15] Rizzi, A.
Numerical Implementation of Solid Body Boundary Conditions for the Euler Equations. ZAMM Vol. 58, pp. 301-304, 1978.

[16] Gottlieb, D. and Turkel, E.
Boundary Conditions for Multistep Finite Difference Methods for Time Dependent Equations.
J. Computational Physics, Vol. 26, pp. 181-196, 1978

[17] Gustafsson, B. and Oliger, J.
Stable Boundary Approximations for a Class of Time Discretizations of u_t = AD u. Upsala University, Dept. of Computer Sciences, Report 87, 1980.

[18] Rudy, D. and Strikwerda, J.
A Non-reflecting Outflow Boundary Condition for Subsonic Navier Stokes Calculations. J. Computational Physics, Vol. 36, pp. 55-70, 1980.

[19] Engquist, B. and Majda, A.
Absorbing Boundary Conditions for the Numerical Simulation of Waves",
Math. Comp. Vol. 31, pp. 629-651, 1977

[20] Bayliss, A. and Turkel, E.
Outflow Boundary Conditions for Fluid Dynamics
ICASE Report 80-21, 1980

[21] Viviand, H. and Veuillot, J.P.
Methods Pseudo-Instationnaires Pour le Calcul D'Ecoulements Transsoniques. ONERA Publication No 1978-4, 1978

[22] Porter, R.W. and Coakley, J.F.
Use of Characteristics for Boundaries in Time Dependent Finite Difference Analysis of Multidimensional Gas Dynamics. Int. J. Num. Meth. in Engineering, Vol. 5, 1972, pp. 91-101

[23] Rizzi, A.W.
Charakteristische Gleichungen für quasi-zeitabhängige Euler Verfahren. Dornier Note BF 30-1496/79, 1979

[24] Grashof, J.
Charakteristikenbeziehungen für die dreidimensionalen zeitabhängigen Euler-Gleichungen bei konstanter Gesamtenthalpie. Dornier Note BF 30-1512/79, 1979

[25] Grashof, J., Schmidt, W. and Rizzi, A.W.
Verfahren zur Berechnung der reibungsfreien Strömung an Überschalleinläufen
DORNIER FB 80/44B, 1980

[26] Mangler, K.W. and Smith, J.H.B.
Behaviour of the Vortex Sheet at the Trailing Edge of a Lifting Wing. RAE TR 69049, 1969

[27] Beam, R.M.
Implicit Numerical Methods for the Compressible Navier Stokes and Euler Equations. VKI-Lecture Series 1982, March 29-April 2, 1982

[28] MacCormack, R.W.
A Numerical Method for Solving the Equations of Compressible Viscous Flow. AIAA-Paper 81-0110, 1981

[29] Garabedian, P.R.
Estimation of the Relaxation Factor for Small Mesh Size. Math Tables Aids Comp., Vol. 10, pp. 183-185, 1956.

[30] South, J.C. and Brandt, A.
Application of a Multi-Level Grid Method to Transonic Flow Calculations. Transonic Flow Problems in Turbomachinery, Hemisphere, Washington, 1977

[31] Jameson, A.
Acceleration of Transonic Potential Flow Calculations on Arbitrary Meshes by the Multiple Grid Method. AIAA Paper 79-1458, 1979

[32] Brandt, A.
Multigrid Solutions to Steady-State Compressible Navier-Stokes Equations I. Proc. 5th Int. Comp. Meth. in Appl. Science and Engin., Dec. 1981

[33] Ni, Ron-Ho.
A Multiple Grid Scheme for Solving the Euler Equations. AIAA-Paper 81-1025, 1981

[34] Naar, M.
Untersuchung zweier moderner Differenzverfahren und ihre Anwendung auf Probleme der Strömungsmechanik Diplomarbeit, Uni Ulm, 1981

[35] Nasa
Numerical Grid Generation Techniques. NASA-CP 2166, 1980

[36] Yu, N.J.
Grid Generation and Transonic Flow Calculations for Three-Dimensional Configurations. AIAA Paper 80-1391, 1980

[37] Lee, K.D.
3-D Transonic Flow Computations Using Grid Systems with Block Structure. AIAA Paper 81-0998

[38] Rizzi, A.W. and Eriksson L.E.
Transfinite Mesh Generation and Damped Euler Equation Algorithm for Transonic Flow Around Wing-Body Configurations. AIAA Paper 81-0999, 1981

[39] Warsi, Z. u. A.
Tensor and Differential Geometry Applied to Analytic and Numerical Coordinate Generation. MSSU-EIRS-81-1, 1981 Mississippi State University

[40] Grashof, J.
Inlet Mesh Generation by Using Maxwell Transformations, Dornier Note, 1982

[41] Salas, M. D.
Rotationally Induced Invisid Wake Bubble.
AIAA 5th CFD Conference Open Forum Paper 10, 1981

[42] Caughey, D.A. and Jameson, A.
Recent Prograss in Finite Volume Calculations for Wing-Fuselage Combinations
AIAA Paper 79 - 1513, 1979

[43] Steger, J. and Warming, R.
Flux Vector Splitting for the Inviscid Gas Dynamic Equations with Application to Finite Difference Methods
NASA TM 78605, 1979

[44] Roe, P.L.
The Use of the Riemann Problem in Finite Difference Schemes. Proceedings of the 7th Int. Conf. on Num. Methods in Fluid Dynamics, Standfort 1980
Springer Verlag, 1981

[45] Roe, P.L.
Numerical Algorithms for the Linear Wave Equation.
Royal Aircraft Establishment Memorandum, 1980

[46] Van Leer, B.
Towards the Ultimate Conservative Differencing Scheme, V, A Second Order Sequel to Godunov's Method
J. Computational Physics, Vol. 32, pp 101 - 126, 1979

[47] Schmidt, W., Jameson, A. Whitfield, D.
Finite Volume Solutions to the Euler Equations in Transonic Flow
To appear in Journal of Aircraft, 1982

[48] Wagner, B.
Estimation of Simulation Errors and Investigations on Operating Range Extensions for the European Transonic Windtunnel ETW
Dornier FB 81 BF/8B, 1981

49 Wagner, B. and Schmidt, W.
Theoretical Investigations of Real Gas Effects in Cryogenic Wind Tunnels
AIAA Journal, Vol. 16, pp. 584 - 586, 1978

50 Haase, W.
Berechnungsverfahren für transsonische Gitterströmungen
Dornier FB 81/BF, 1981

51 Grashof, J. and Schmidt, W.
Computational Method for Two- and Three-Dimensional Inlets in Subsonic and Supersonic Flow
ICAS Congress 1982, Seattle, August 1982

52 Manro, M.E., Manning, K.J.R., Hallstaff, T.H. and Rogers, J.T.
Transonic Pressure Measurements and Comparison of Theory to Ecperiment for an Arrow-Wing Configuration
NASA-CR-2610, 1976

53 Schmidt,W., Jameson, A.
Euler Solutions as Limit of Infinite Re-Number For Separated Flows and Flows with Vortices
Paper to be given at the 8th Int. Conf. on Num. Methods in Fluid Dynamics, Aachen 1982

54 Eriksson, L.E. and Rizzi, A.W.
Computational Study of Vortex Flow at a Wing Tip Using Euler Equations and a Tip-Conformal Mesh
Gamm-Conference, Paris, Oct. 1981

55 Jameson, A., Schmidt, W., Turkel, E.
Numerical Solutions fo the Euler Equations by Finite Volume Methods Using Runge Kutte Tim Stepping Schemes
AIAA-Paper 1259, June 1981

11. FIGURES

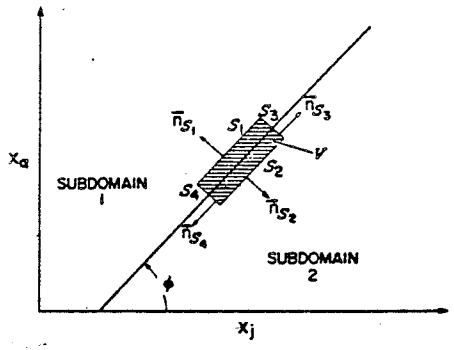

Two subdomains separated by a surface at which the solution F_α is discontinuous.

Fig. 1

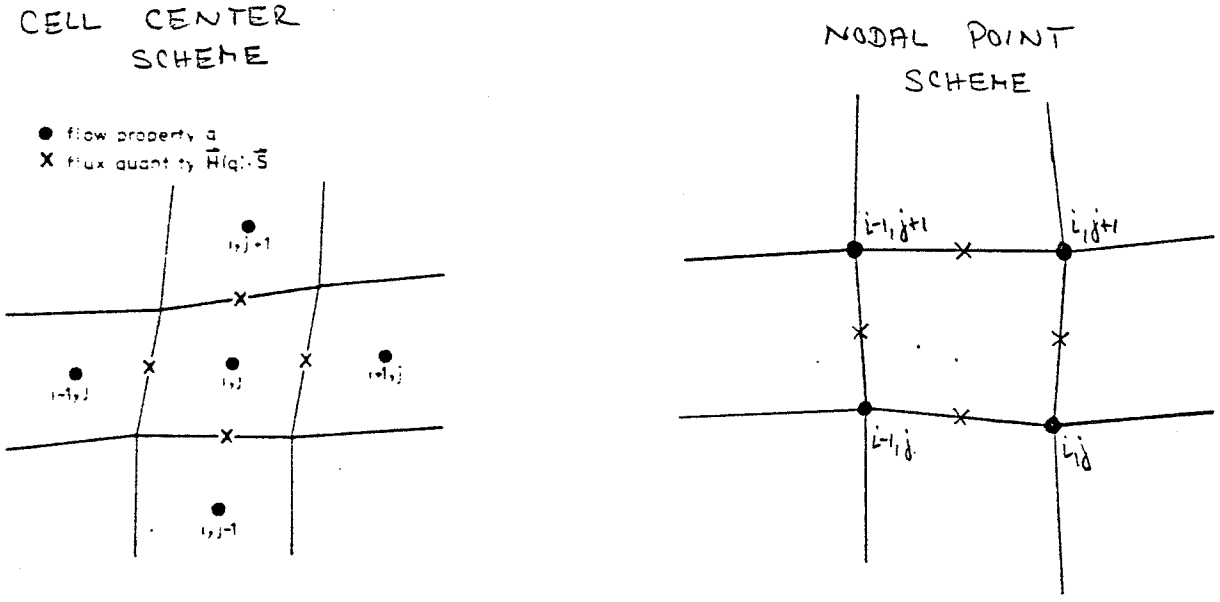

Fig. 2

$P_{T,1}=P_{T,2}$ $P_1=P_2$ $Q_1=0.$ $Q_2=0.$ $P_{T,1}\leq P_{T,2}$ $P_1=P_2$ $Q_1=0.$ $Q_2\geq 0.$

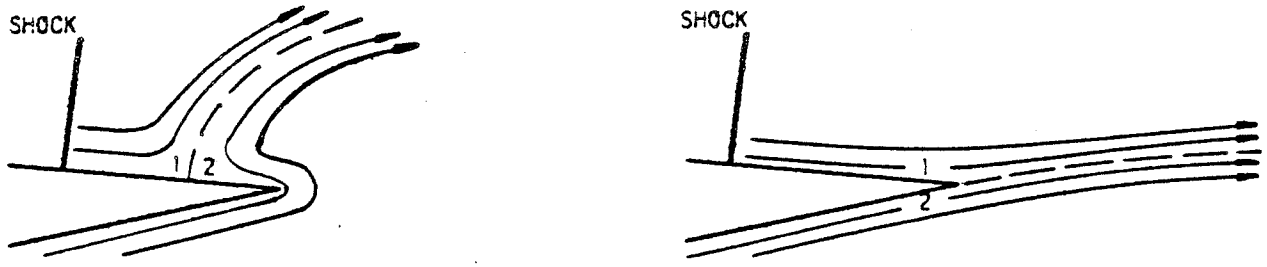

A) POTENTIAL FLOW B) EULER FLOW

TRANSONIC

TRAILING EDGE FLOW BEHAVIOUR (FULL POTENTIAL - EULER)

$P_{T,1}=P_{T,2}$ $P_1=P_2$ $Q_1=0.$ $Q_2=0.$ $P_{T,1}=P_{T,2}$ $P_1=P_2$ $Q_1=0.$ $Q_2=0.$

A) POTENTIAL FLOW B) EULER FLOW

SUBSONIC

TRAILING EDGE FLOW BEHAVIOUR (FULL POTENTIAL - EULER)

Fig. 3

THREE - STAGE SCHEME

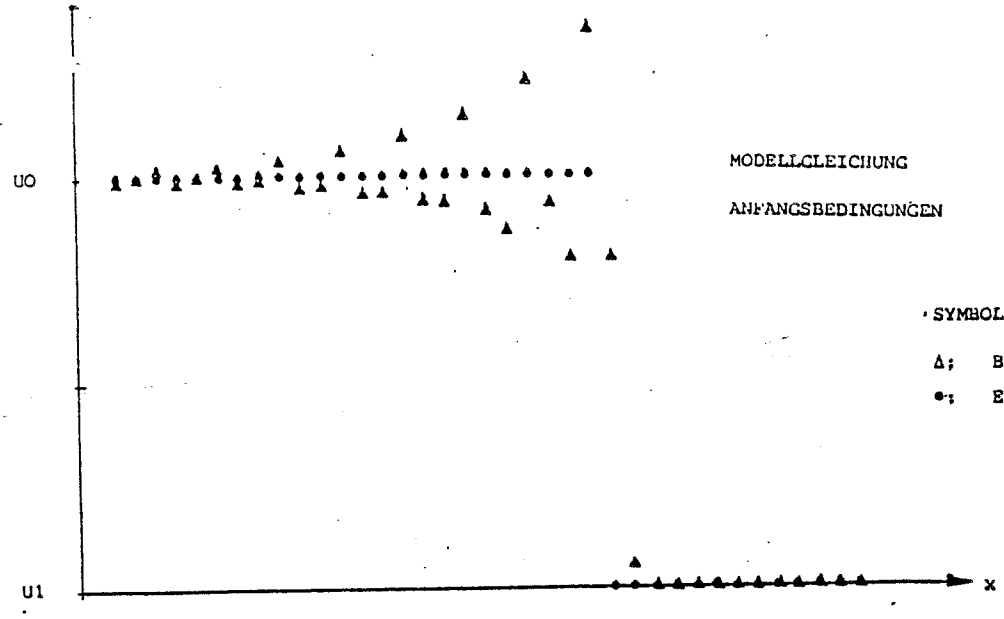

SHOCK SOLUTION NO FILTER

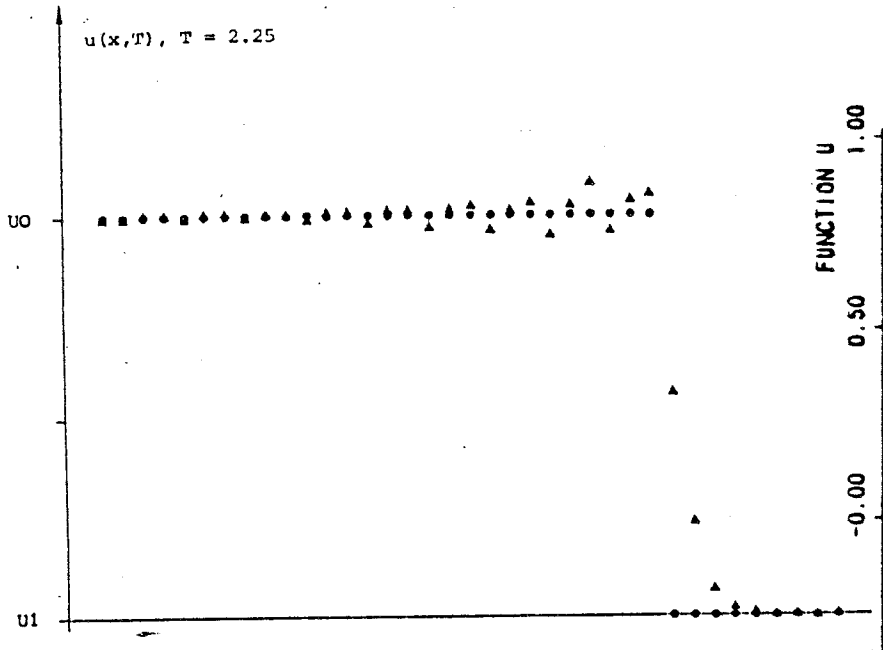

SHOCK SOLUTION $\varepsilon^{(2)}$ - FILTER

BURGERS EQUATION

Fig. 5

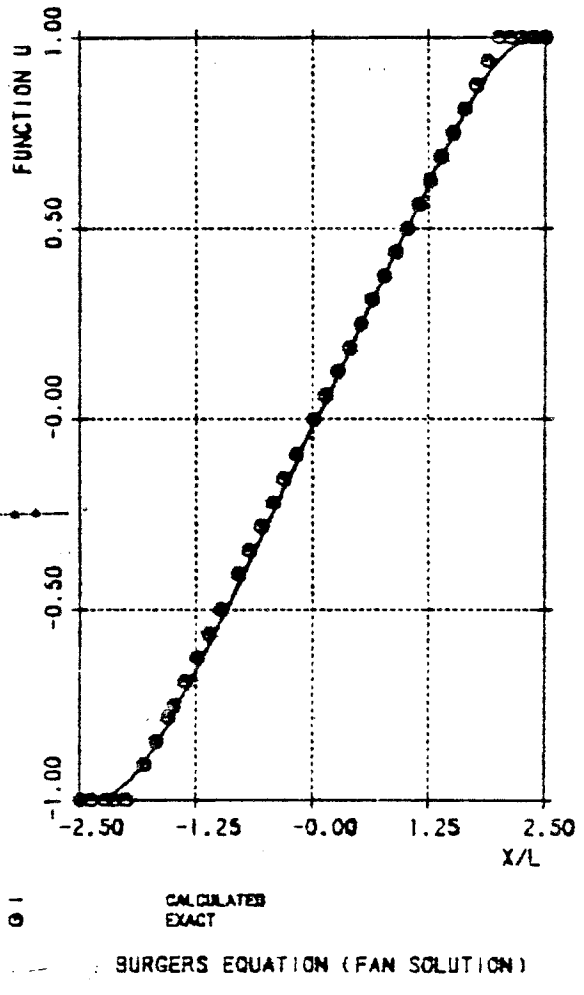

Fig. 4

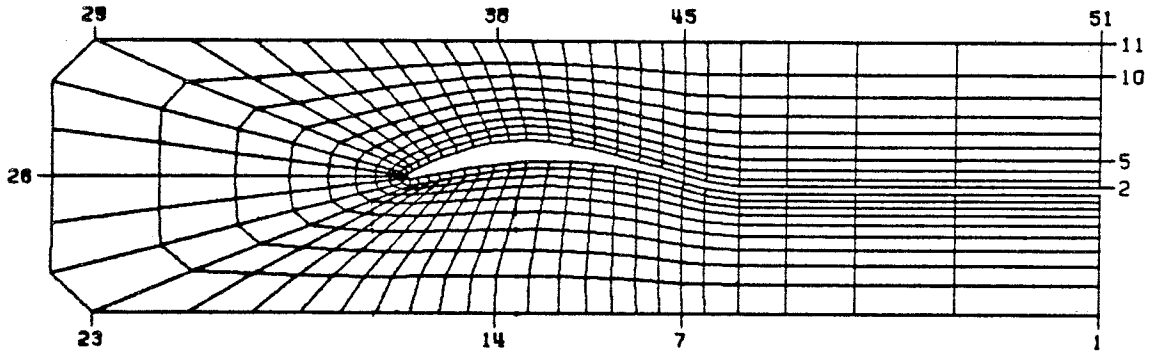

MESH FOR FLOW BETWEEN WALLS

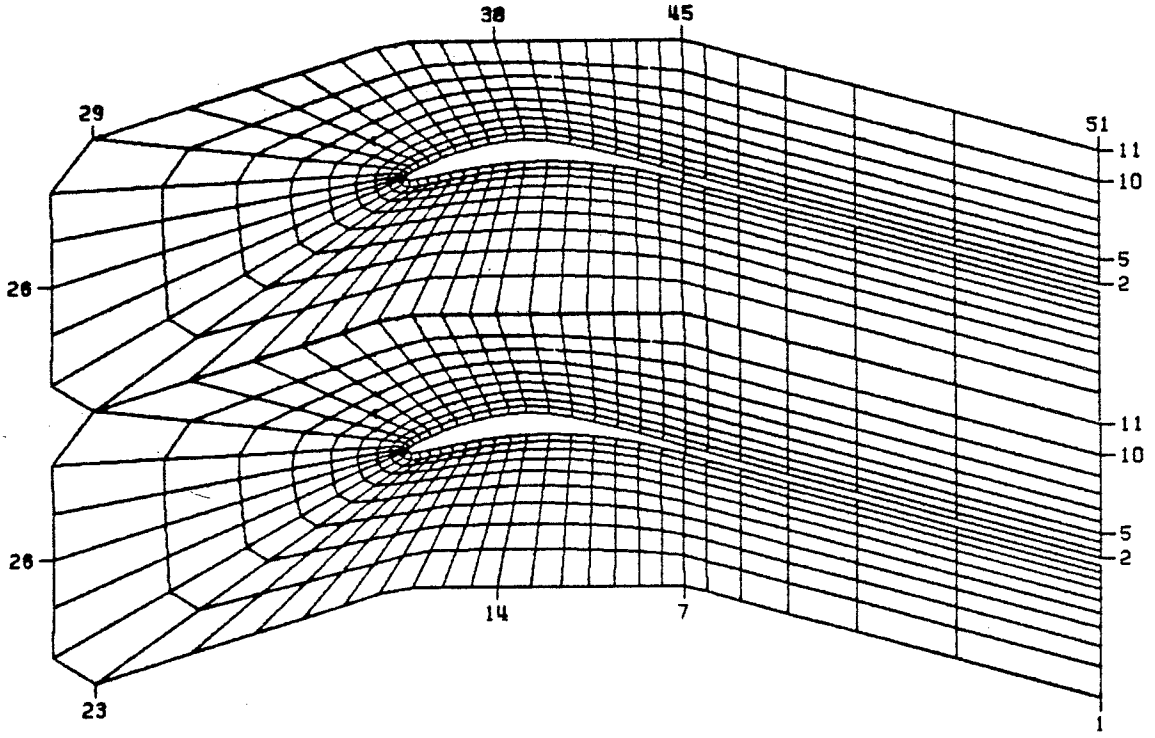

TURBOMACHINERY CASCADE MESH

Fig. 6

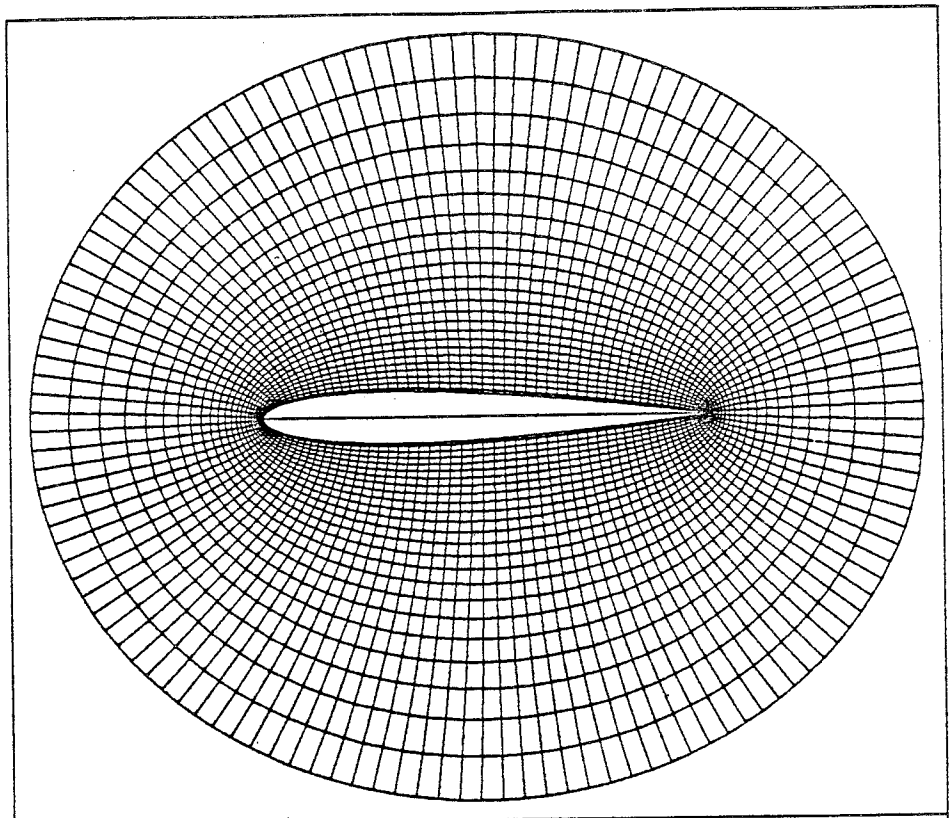

Fig. 7

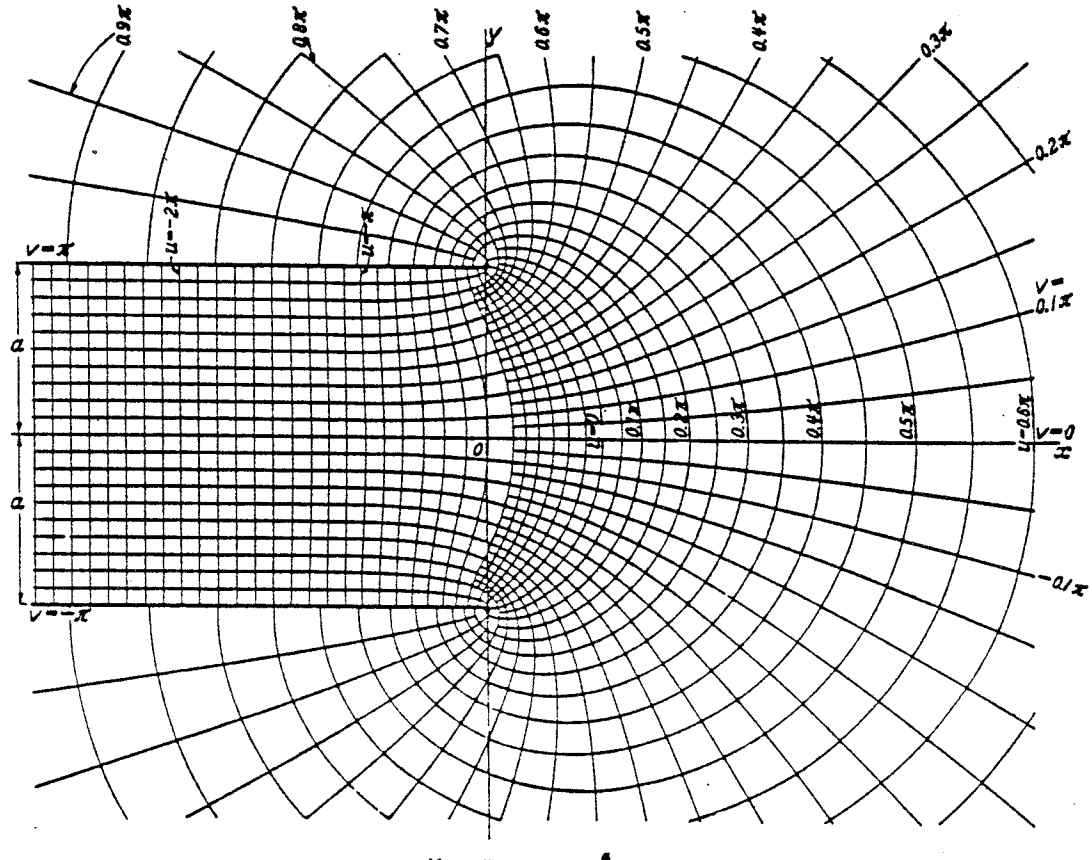

Maxwell curves, $z = \frac{a}{\pi}(w + 1 + e^{w})$

Fig. 8

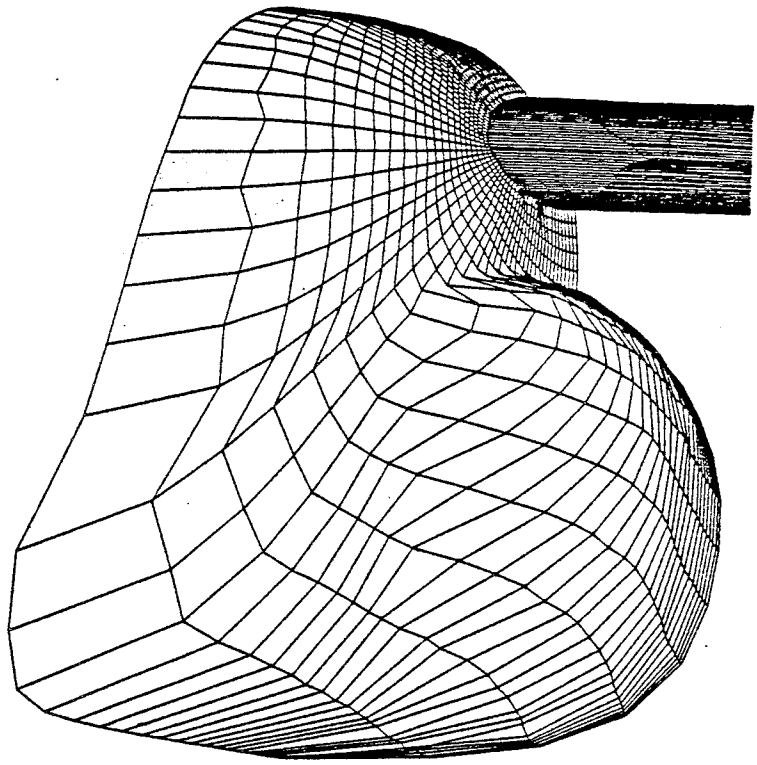

DORNIER

MESH-GENERATION FOR
TRANSONIC TRAINER AIRCRAFT

C-H MESH

Fig. 9

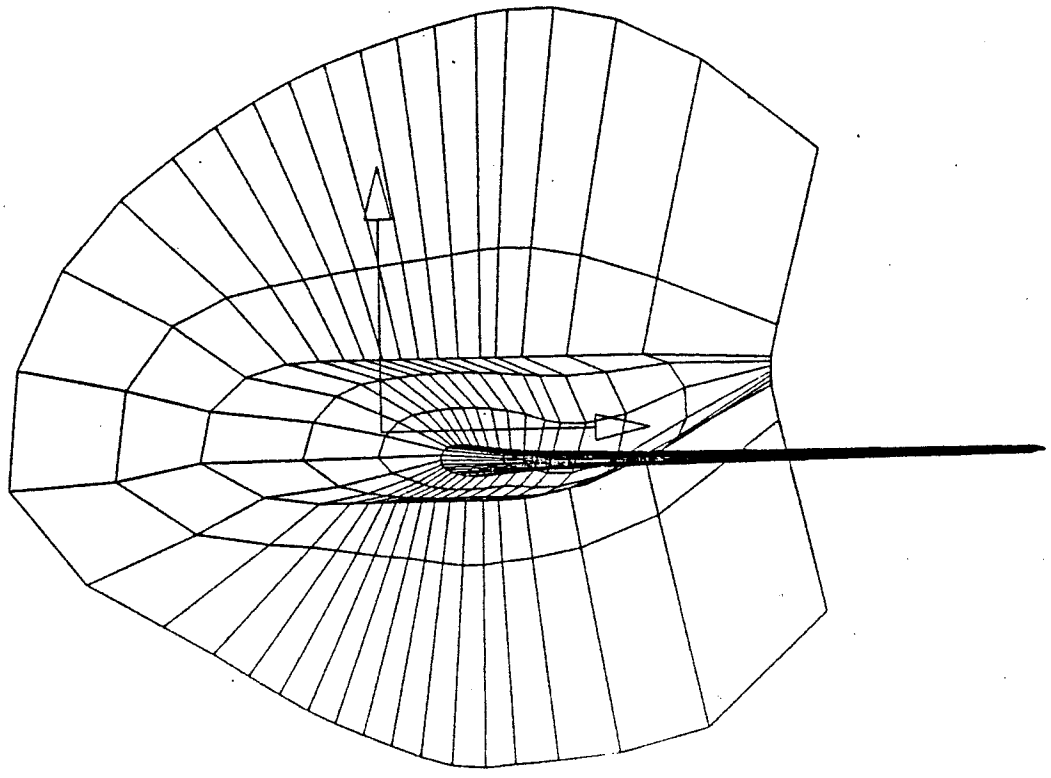

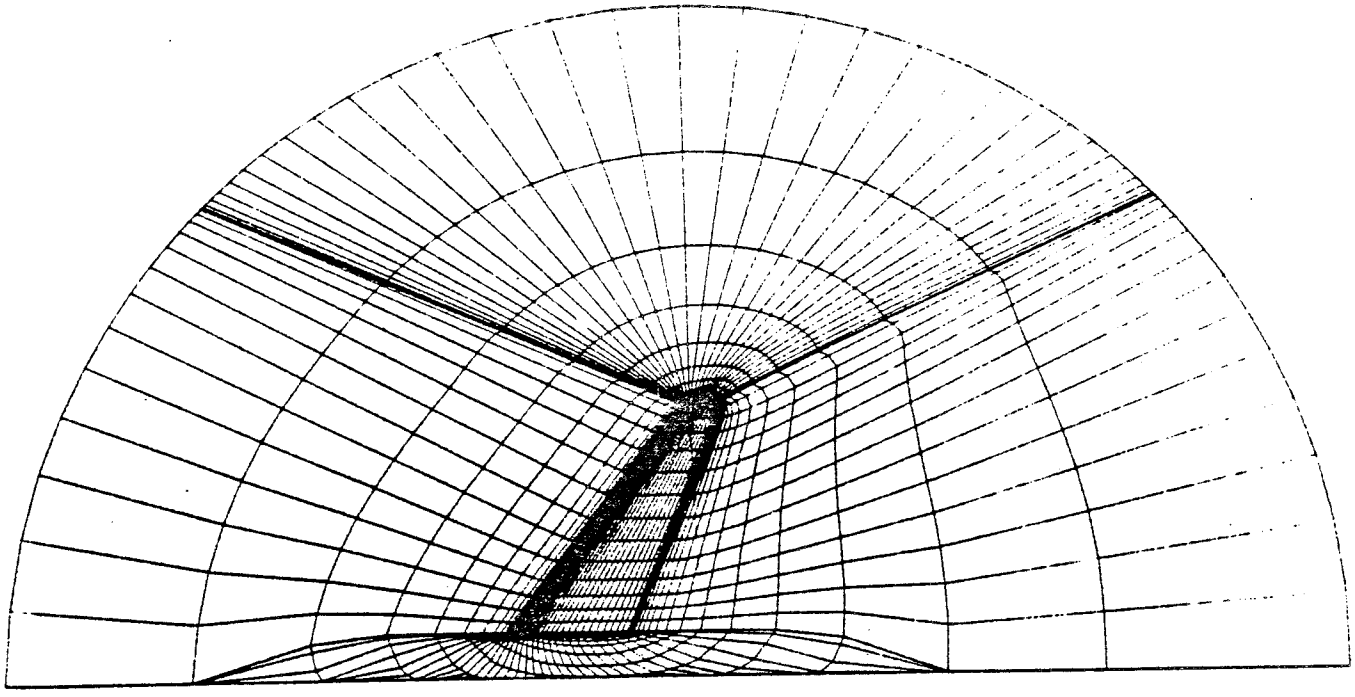

O-O MESH

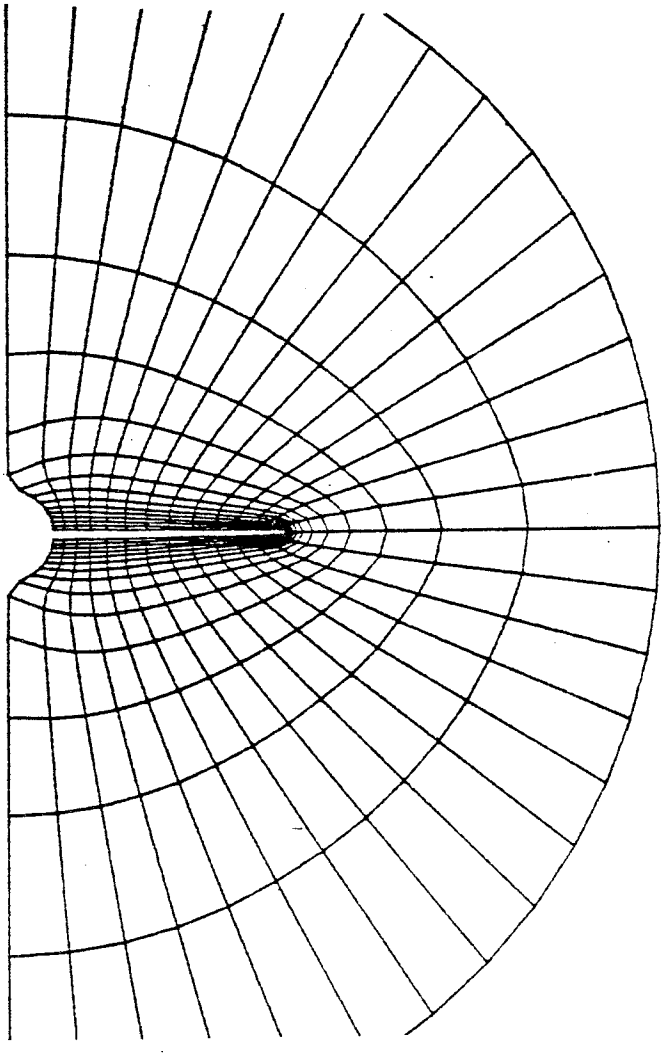

Fig. 9

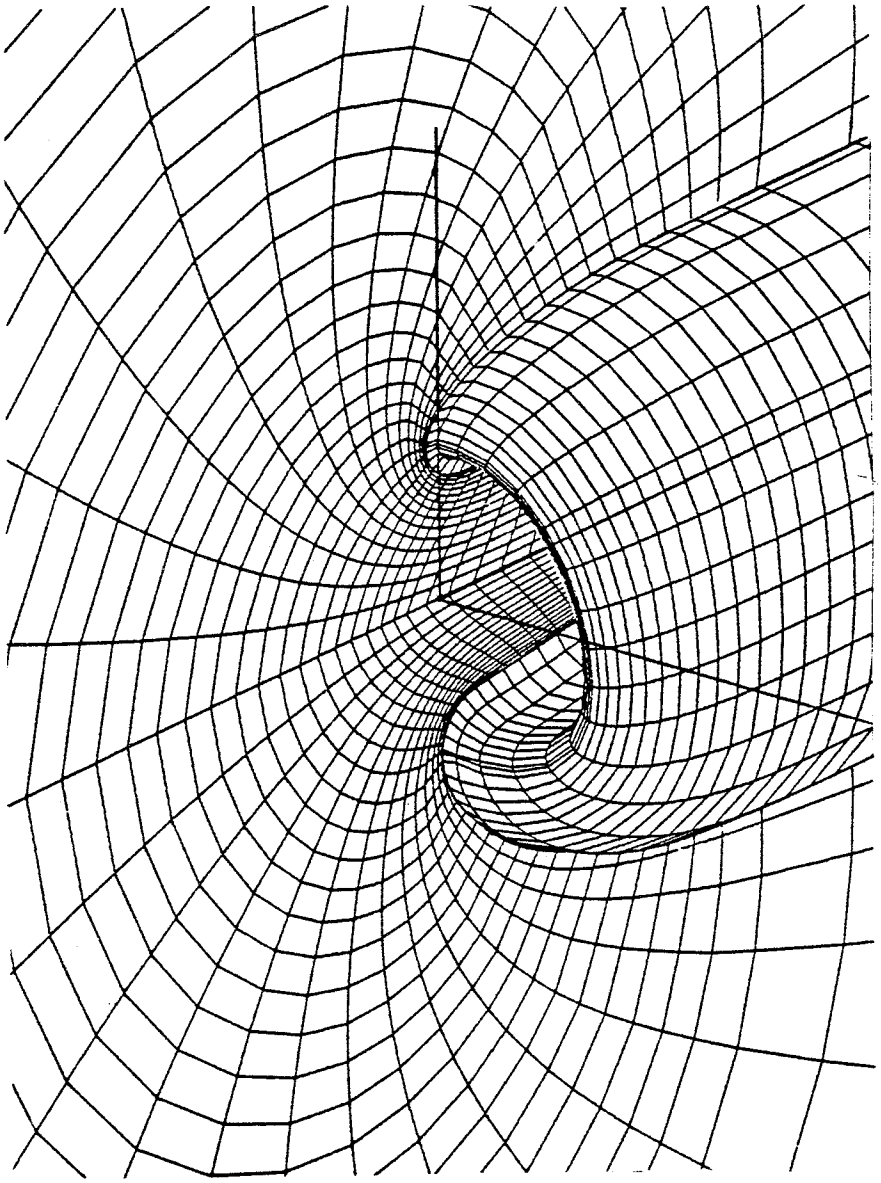

DORNIER

MESH-GENERATOR FOR
THREE-DIMENSIONAL INLETS

Fig. 10

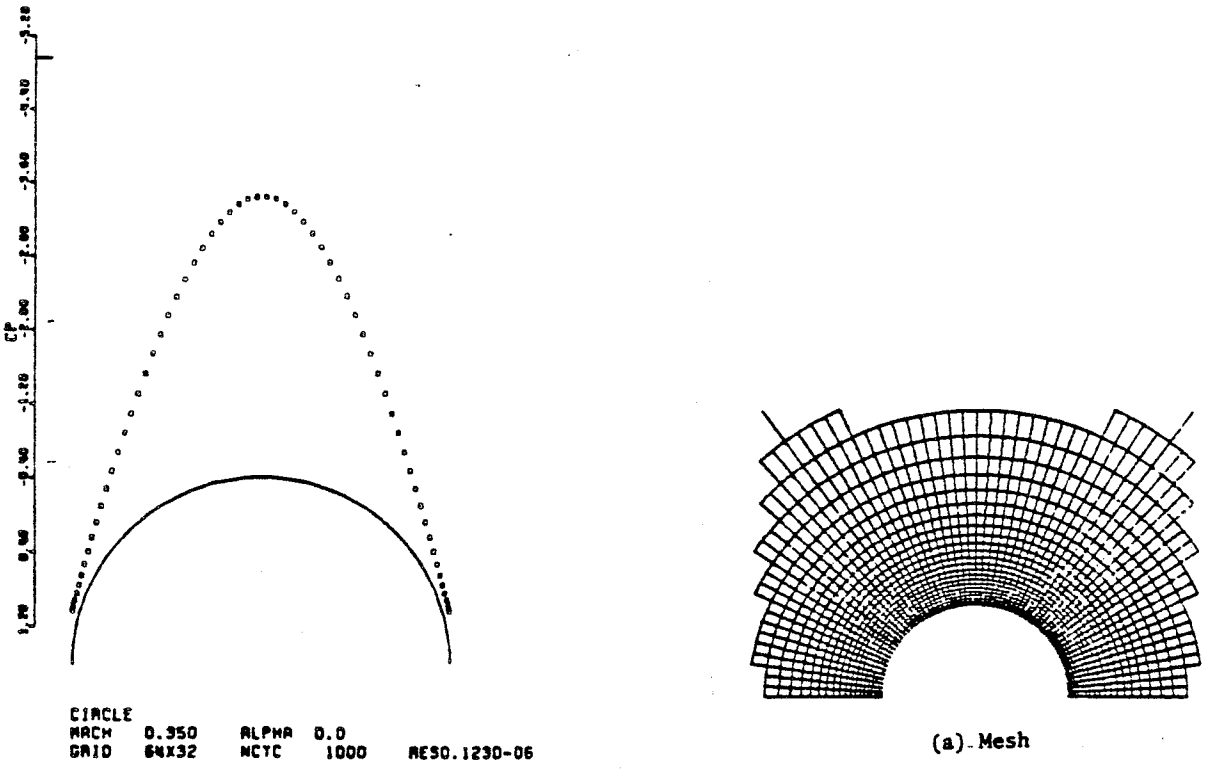
CP
CIRCLE
MACH 0.350 ALPHA 0.0
GRID 64X32 NCYC 1000 RES0.1230-06
(a) Mesh

Fig. 11

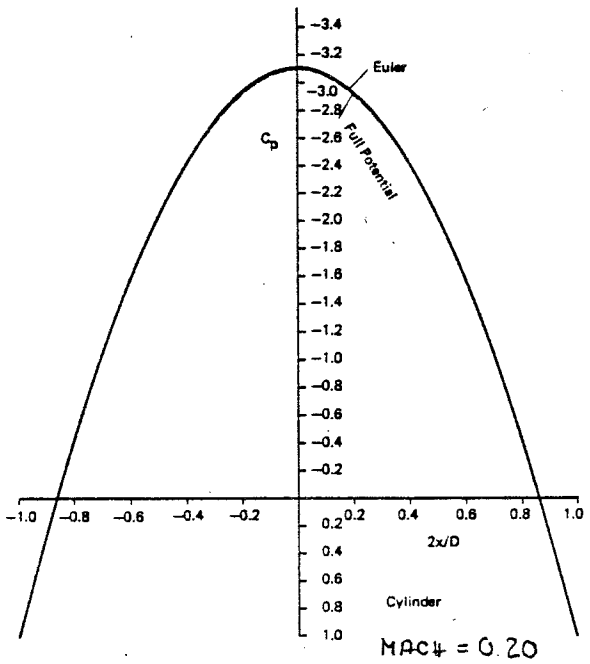
Euler
Full Potential
C_p
2x/D
Cylinder
MACH = 0.20

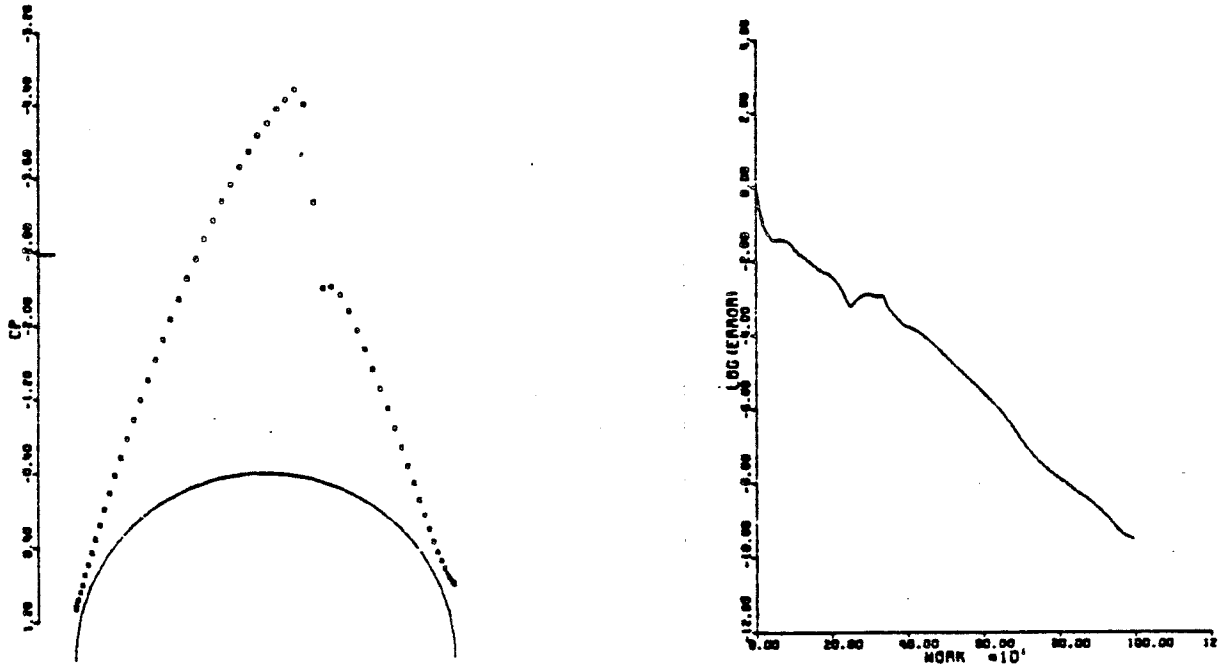
CP
LOG (ERROR)
NORK *10⁴
CIRCLE
MACH 0.450 ALPHA 0.0
GRID 64X32 NCYC 1000 RESO.48
CIRCLE
MACH 0.450 ALPHA 0.0
RESID1 0.1670+01 RES102 0.4860-09
NORK 999.00 RATE 0.9783
GRID 64X32

Fig. 12

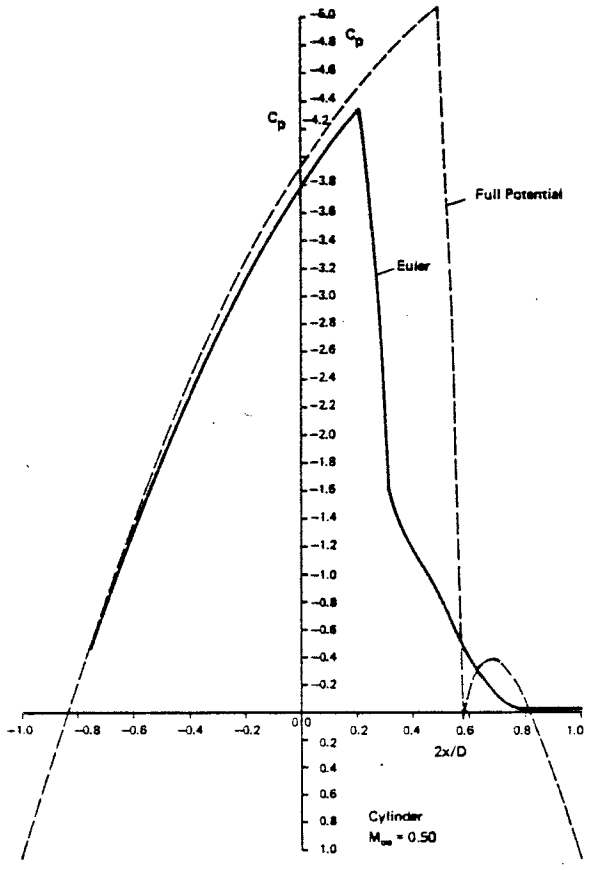
C_p
C_p
Full Potential
Euler
2x/D
Cylinder
M_∞ = 0.50

Fig. 13

CYLINDER MACH = 0.50

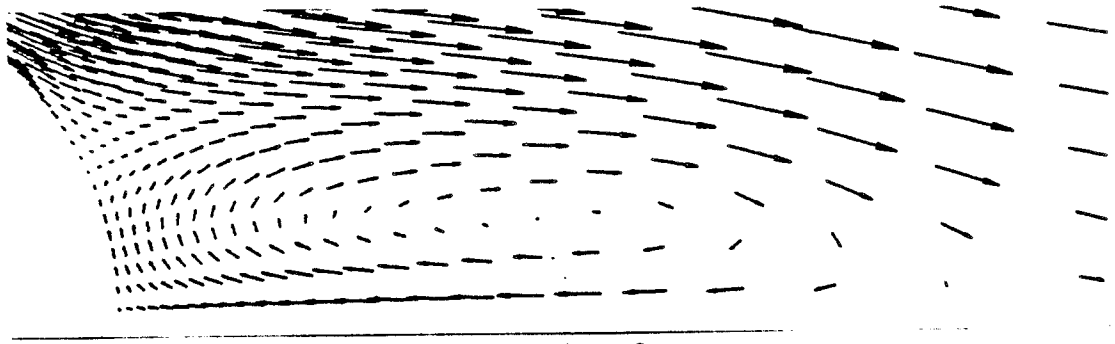

VELOCITY - VECTOR

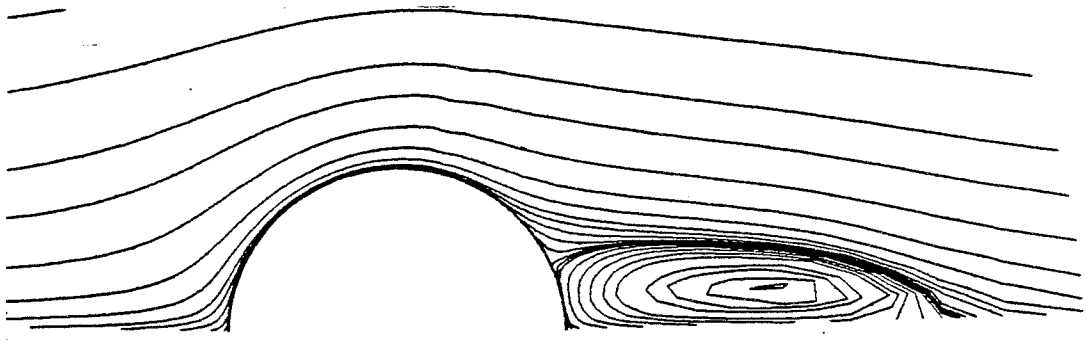

STREAMLINES

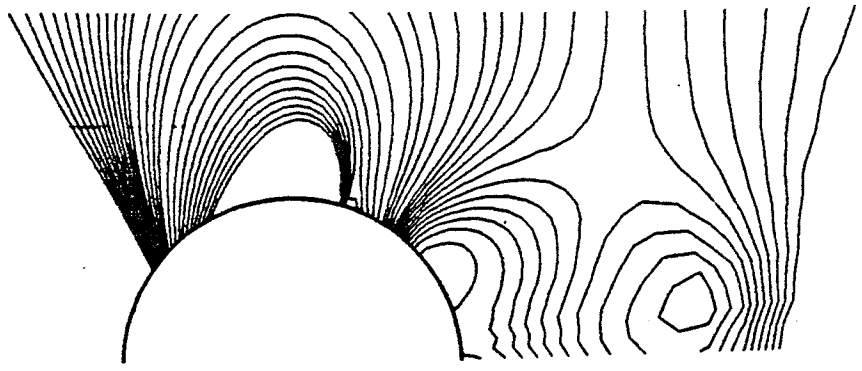

ISOBARS

Fig. 13

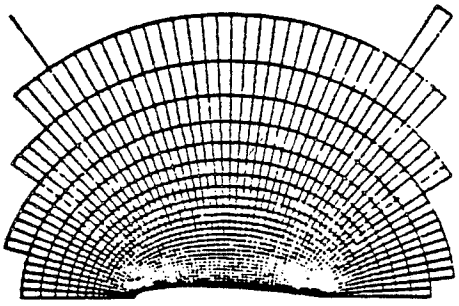

(a) Mesh

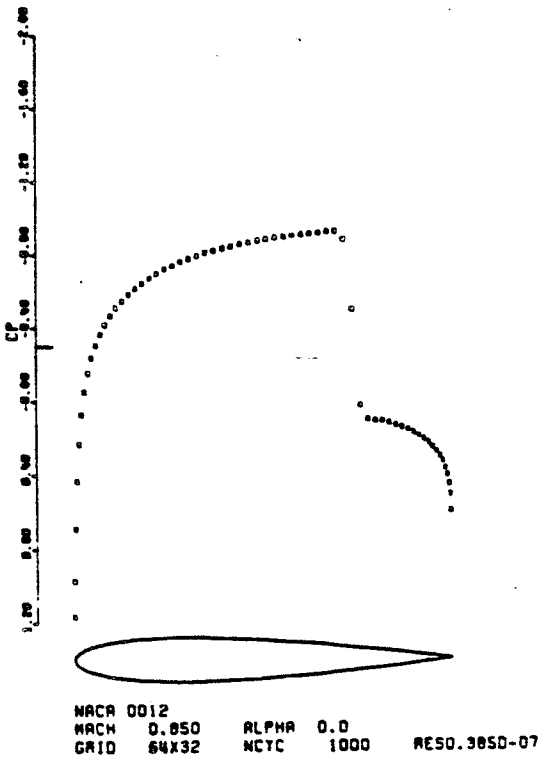

(c) Euler equations

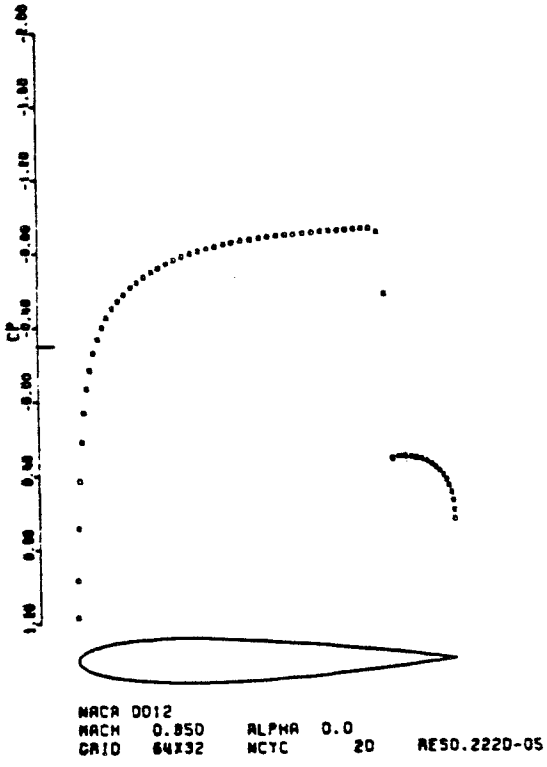

(b) Potential flow

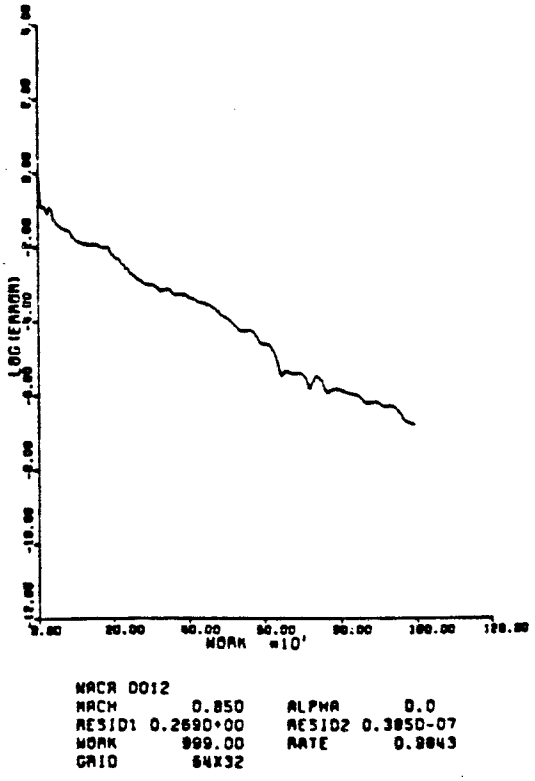

(d) Convergence history

Fig. 14

NACA 0012 airfoil at Mach .85

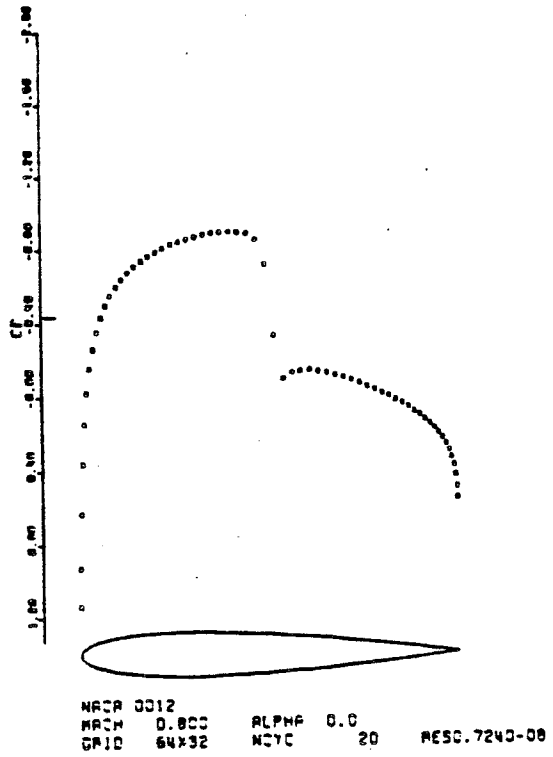

(a) Potential flow

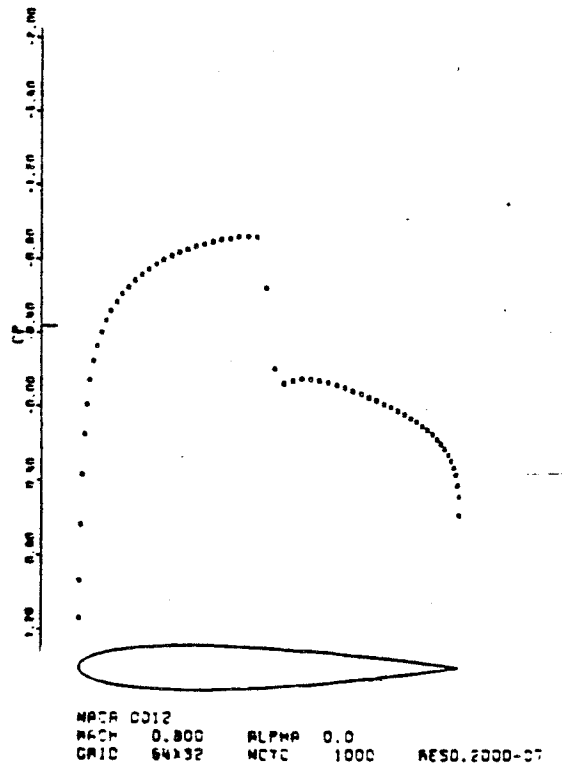

(b) Euler equations

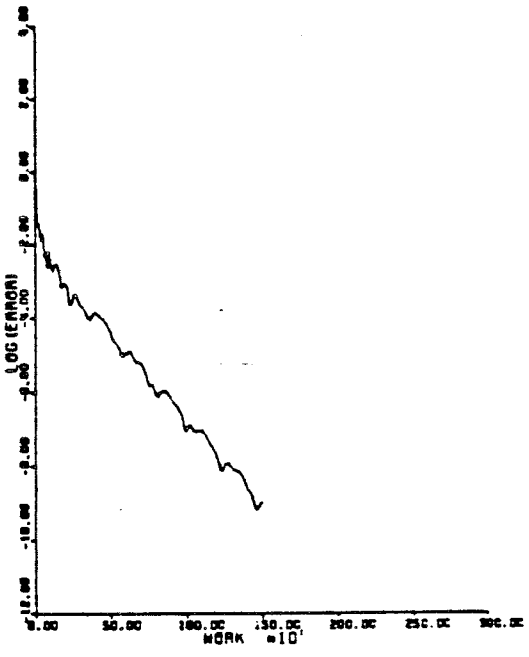

(c) Convergence with enthalpy damping

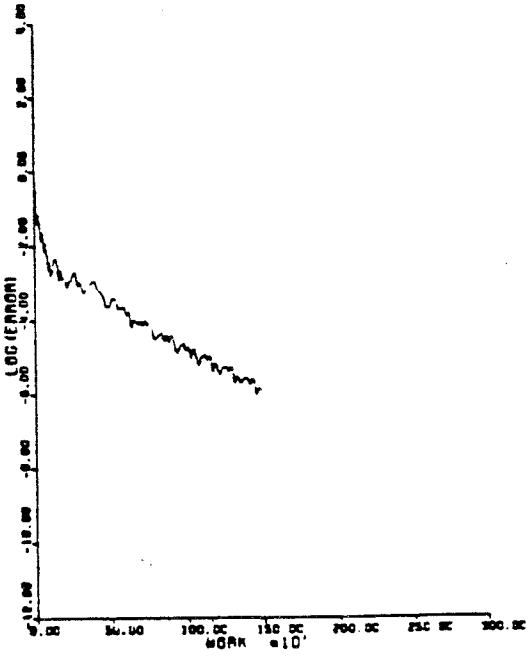

(d) Convergence without enthalpy damping

Fig. 15

NACA 0012 airfoil at Mach .80

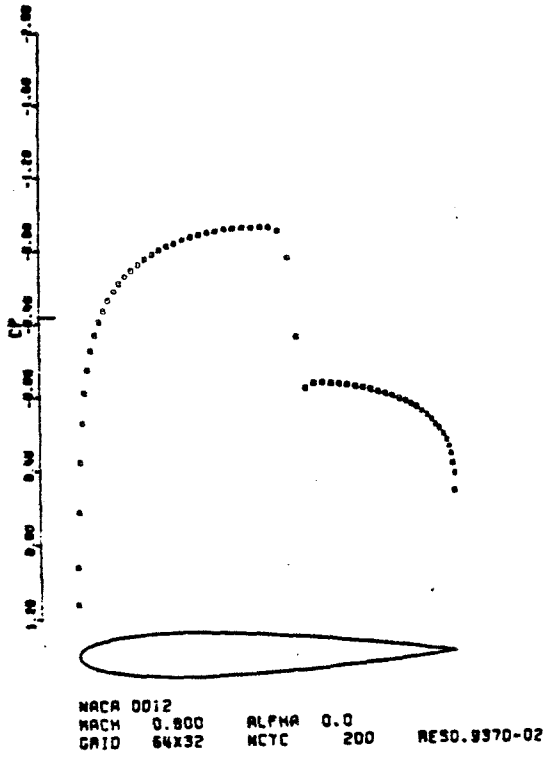

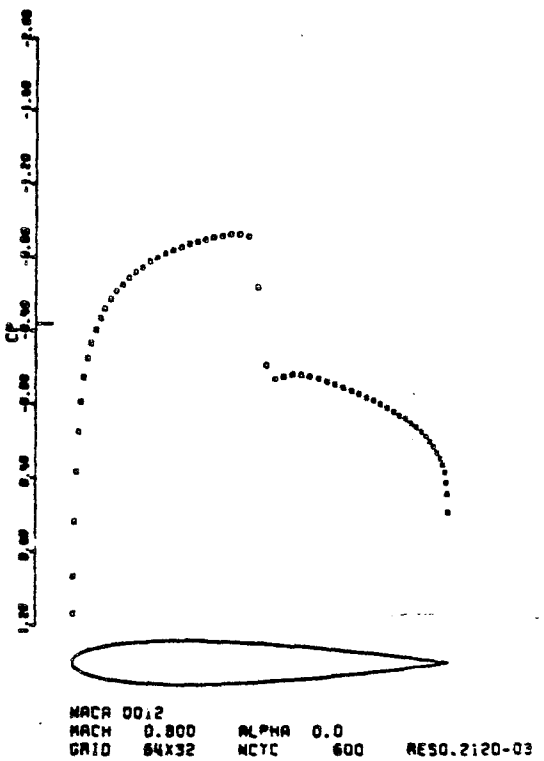

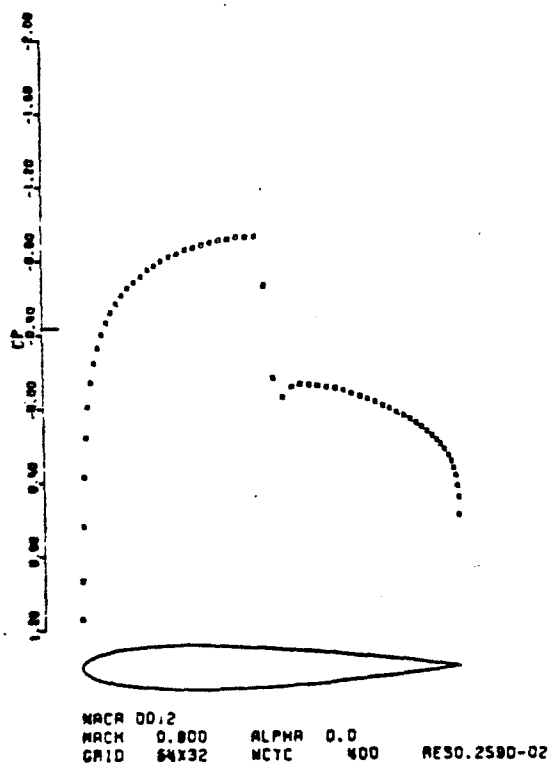

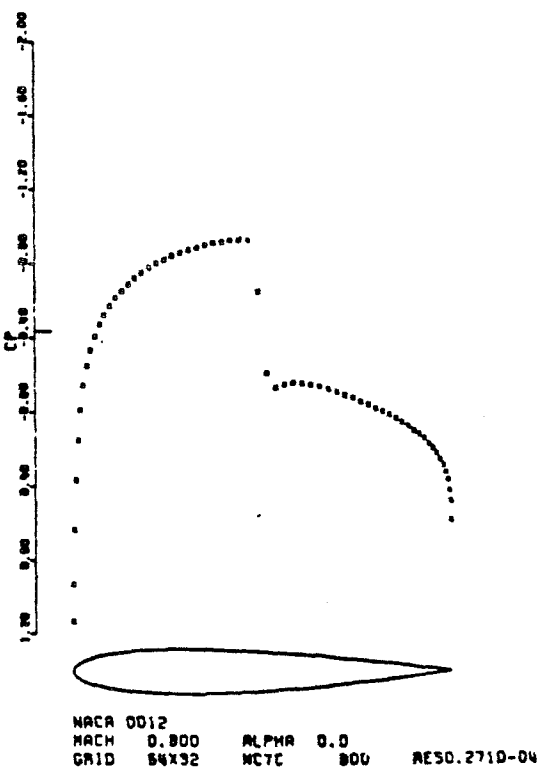

Fig. 16

Development of flow field: NACA 0012 airfoil at Mach .80

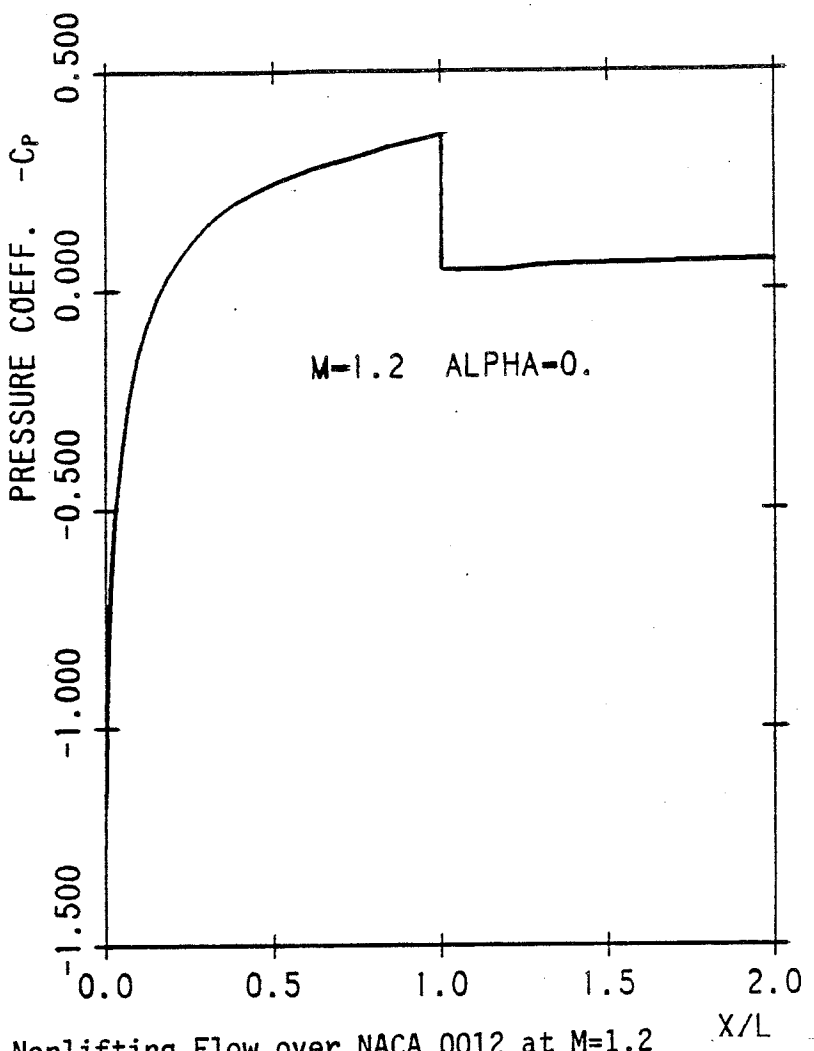

Nonlifting Flow over NACA 0012 at M=1.2

Fig. 17

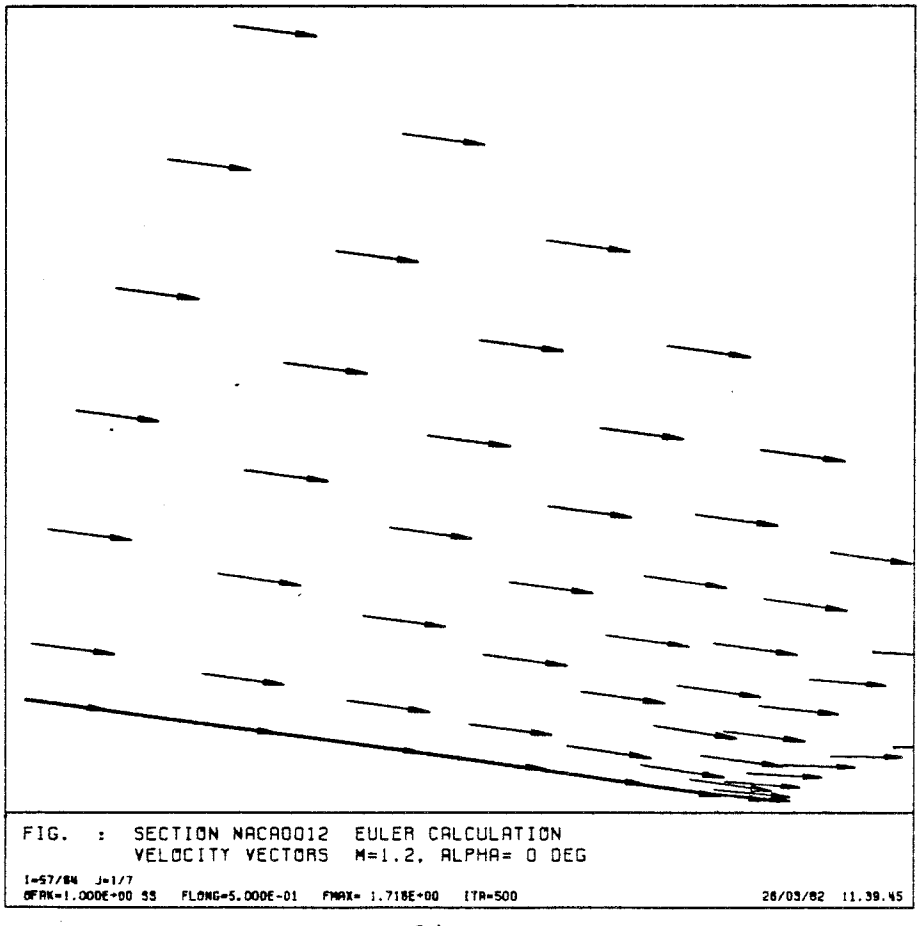

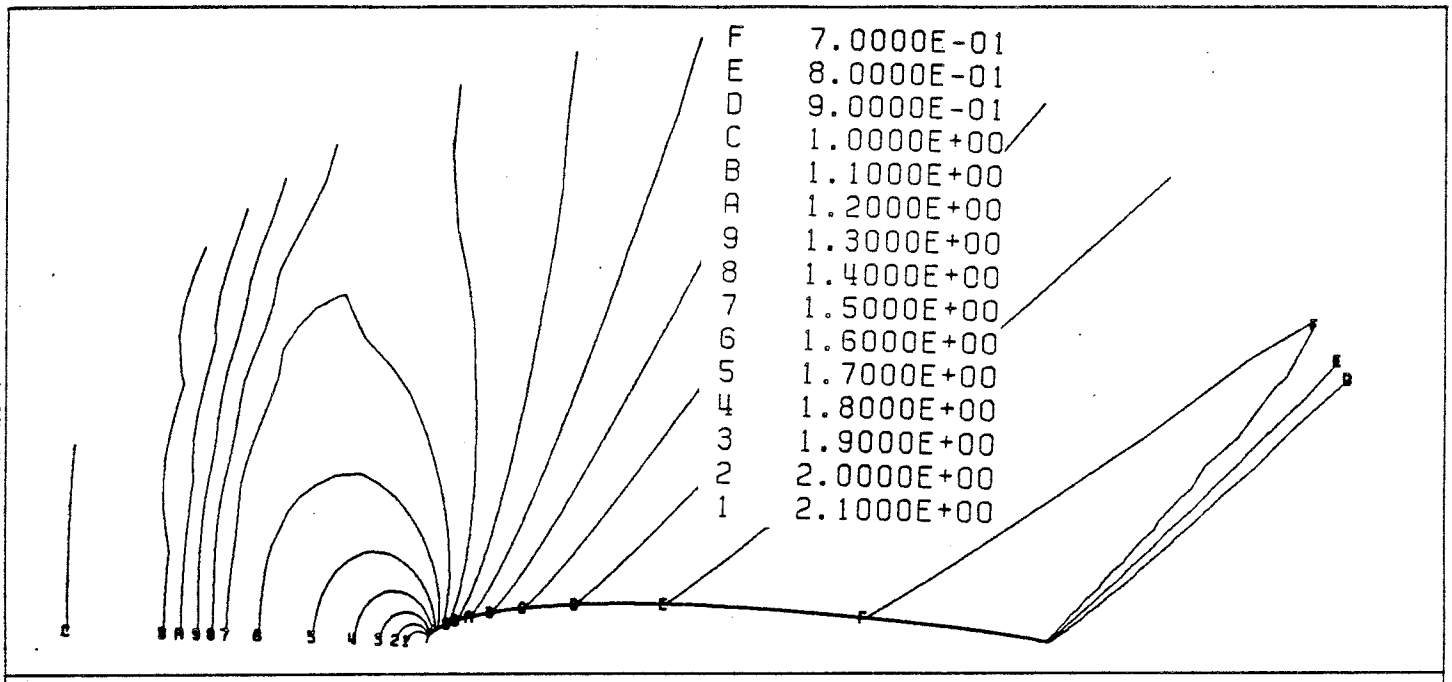

FIG. : SECTION NACA0012 EULER CALCULATION
ISOBARS M=1.2, ALPHA= 0 DEG

I=1/64 J=1/25
DFAK=1.000E+00 FLONG=0.000E+00 FMAX= 2.388E+00 FMIN= 6.071E-01 ITA=500 26/03/82 12.47.37

Fig. 17

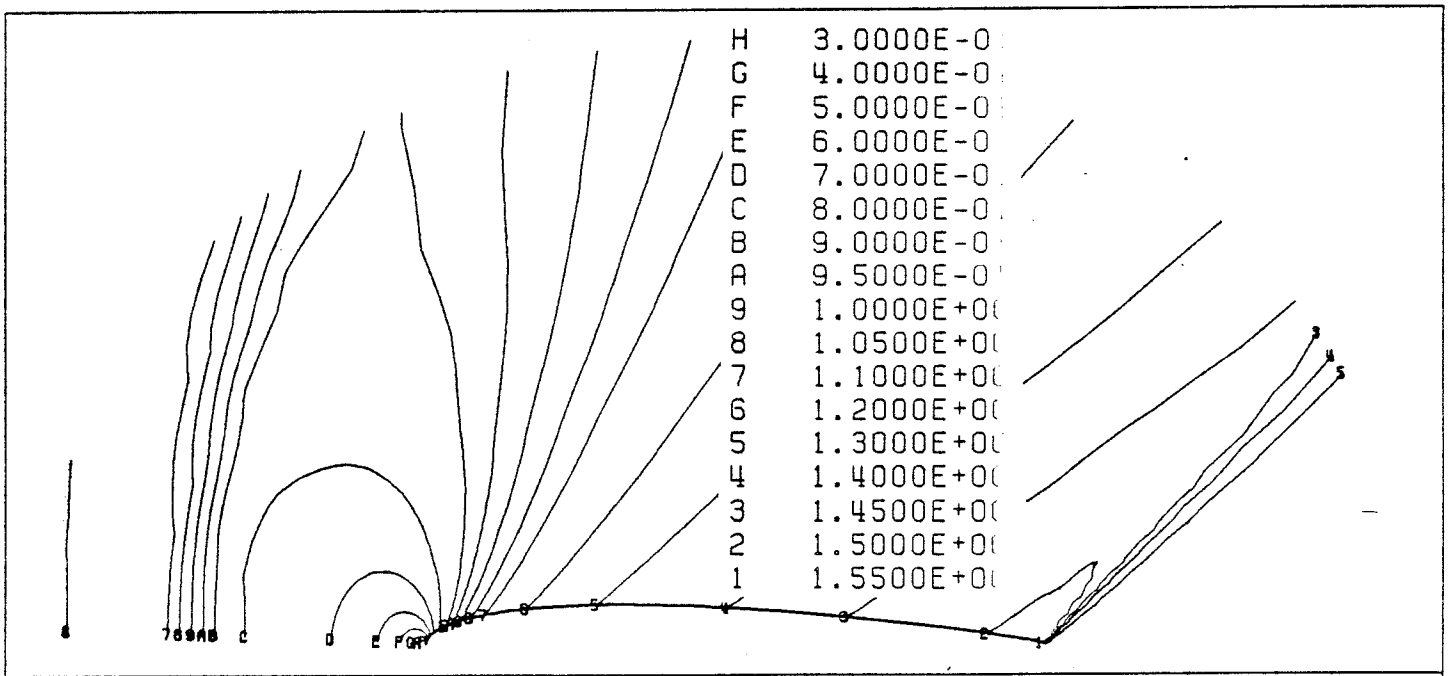

FIG. : SECTION NACA0012 EULER CALCULATION
LINES MACH=CONST. M=1.2, ALPHA= 0 DEG

I=1/64 J=1/25
DFAK=1.000E+00 FLONG=0.000E+00 FMAX= 1.557E+00 FMIN= 1.082E-01 ITA=500 26/03/82 13.01.29

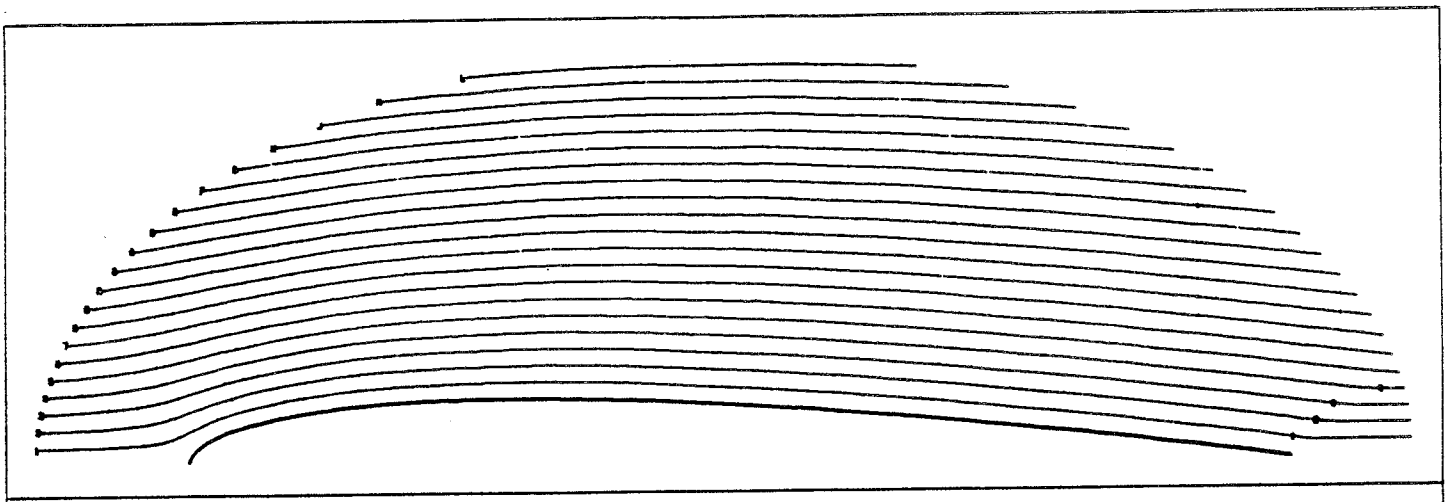

FIG. : SECTION NACA0012 EULER CALCULATION
STREAMLINES M=1.2, ALPHA= 0 DEG

I=1/64 J=1/17
DFAK=1.000E+00 FLONG=0.000E+00 FMAX= 4.493E-01 FMIN= 0.000E+00 ITA=500 26/03/82 11.56.54

Fig. 17

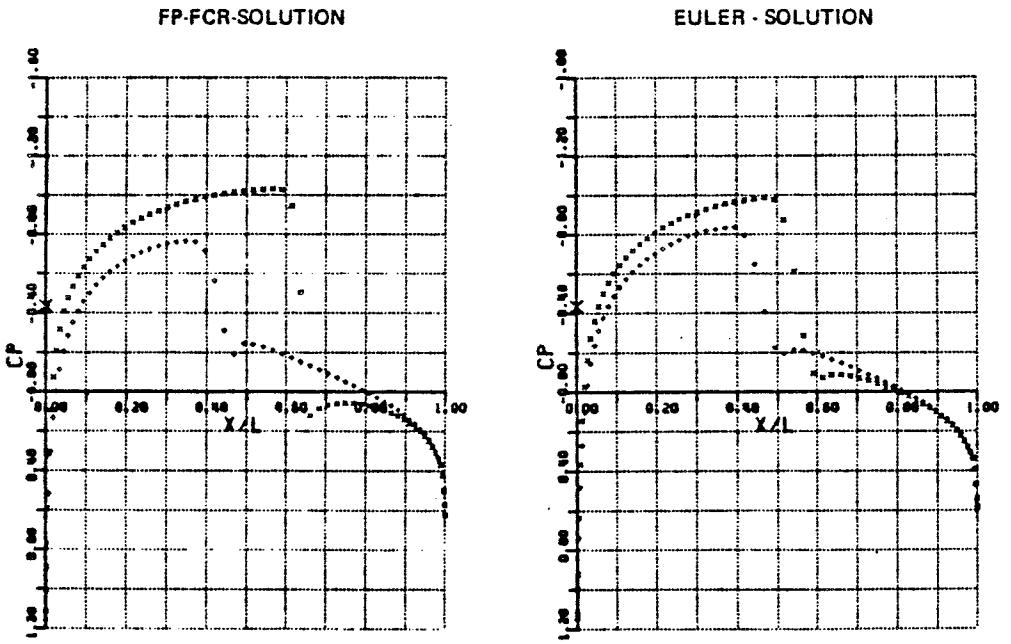

NACA 0012, M_∞= 0.80, α = 0.37°

CL= 0.220560 CD= 0.012940 CM= 0.046583 CL= 0.105143 CD= 0.010324 CM= 0.018166

Fig. 18

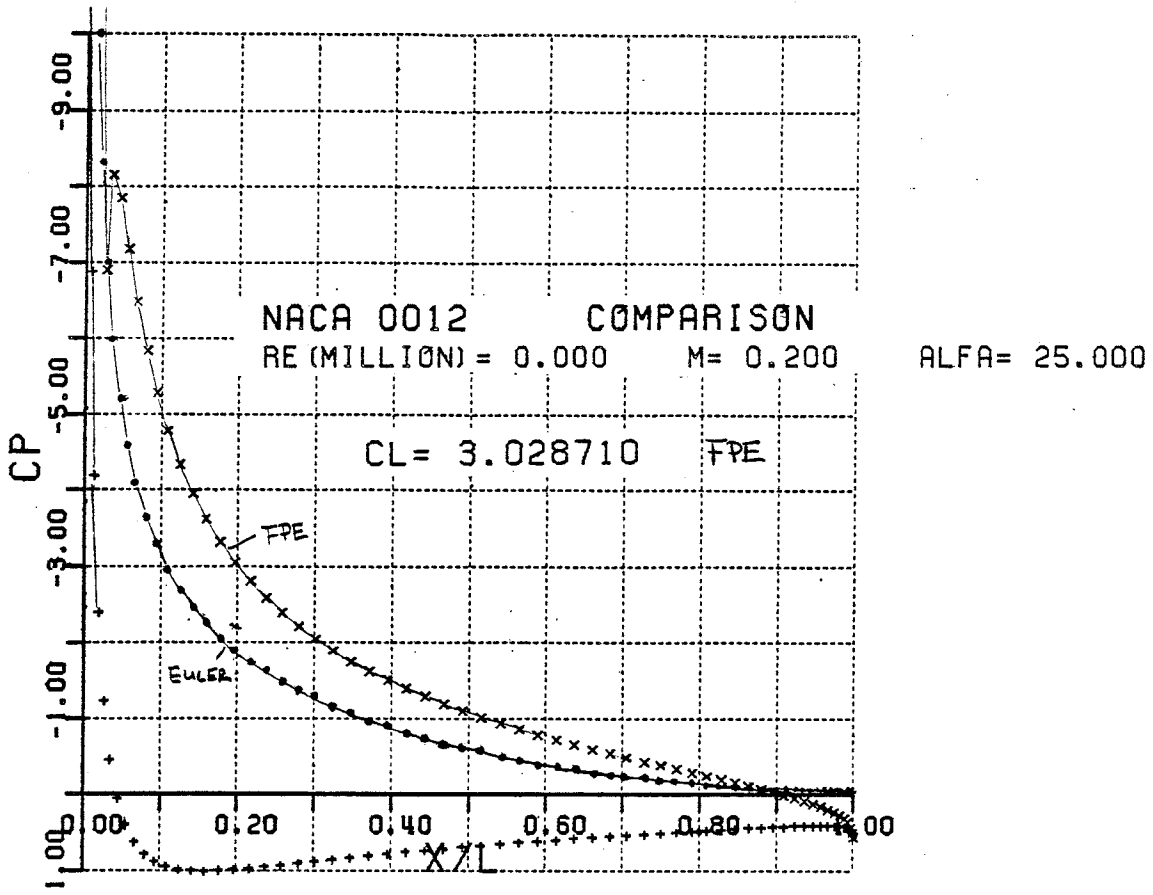

MAX. VALUE= 33.095664 FPE
15.735 EULER

Fig. 19

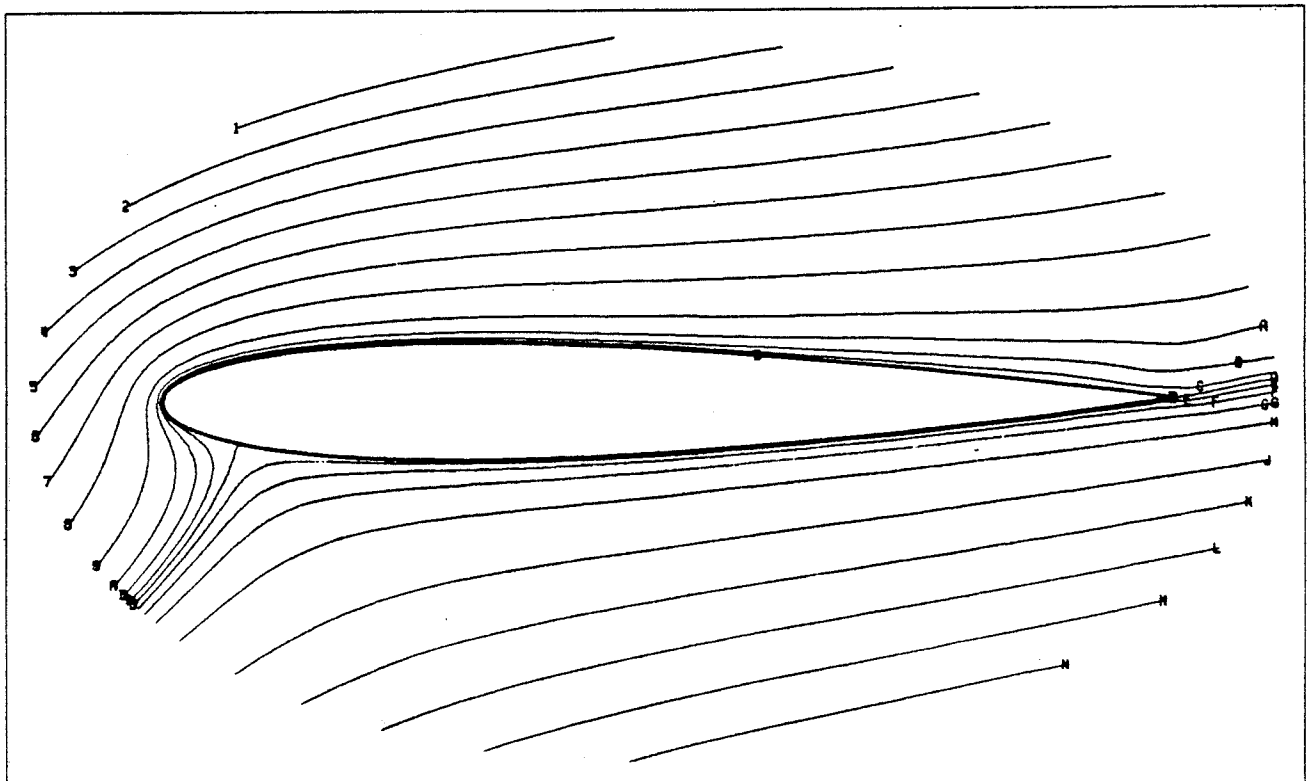

FIG. : SECTION NACA0012 EULER CALCULATION
STREAMLINES M=0.2, ALPHA= 25 DEG

I=1/130 J=1/17
DFAK=1.000E+00 SS FLONG=0.000E+00 FMAX= 9.440E-02 FMIN=-6.633E-02 ITA=500 26/03/82 16.58.42

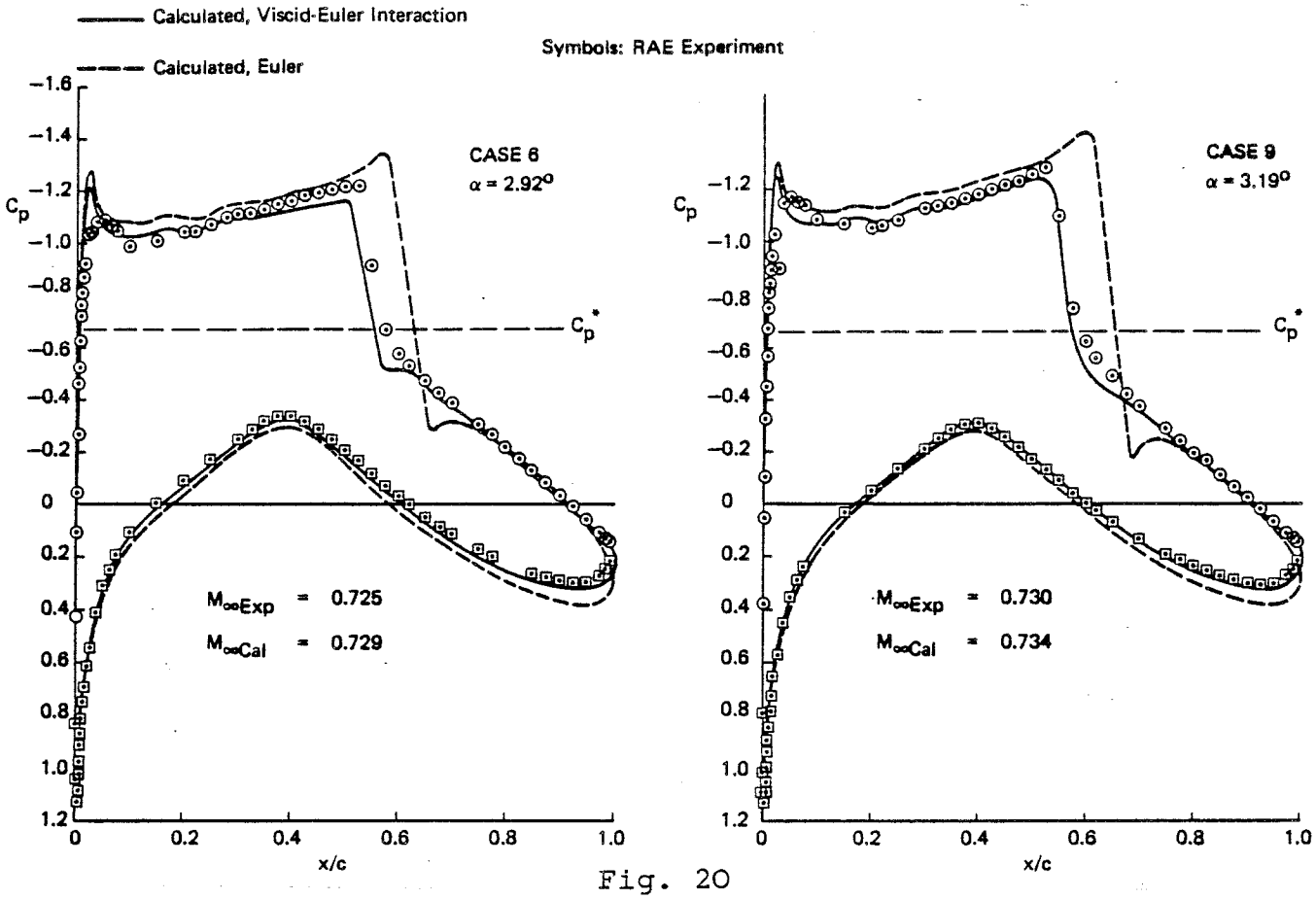
Calculated, Viscid-Euler Interaction
Calculated, Euler
Symbols: RAE Experiment
CASE 6
α = 2.92°
CASE 9
α = 3.19°
C_p
C_p^*
$M_{\infty Exp}$ = 0.725
$M_{\infty Cal}$ = 0.729
$M_{\infty Exp}$ = 0.730
$M_{\infty Cal}$ = 0.734
x/c

Fig. 20

Fig. 21

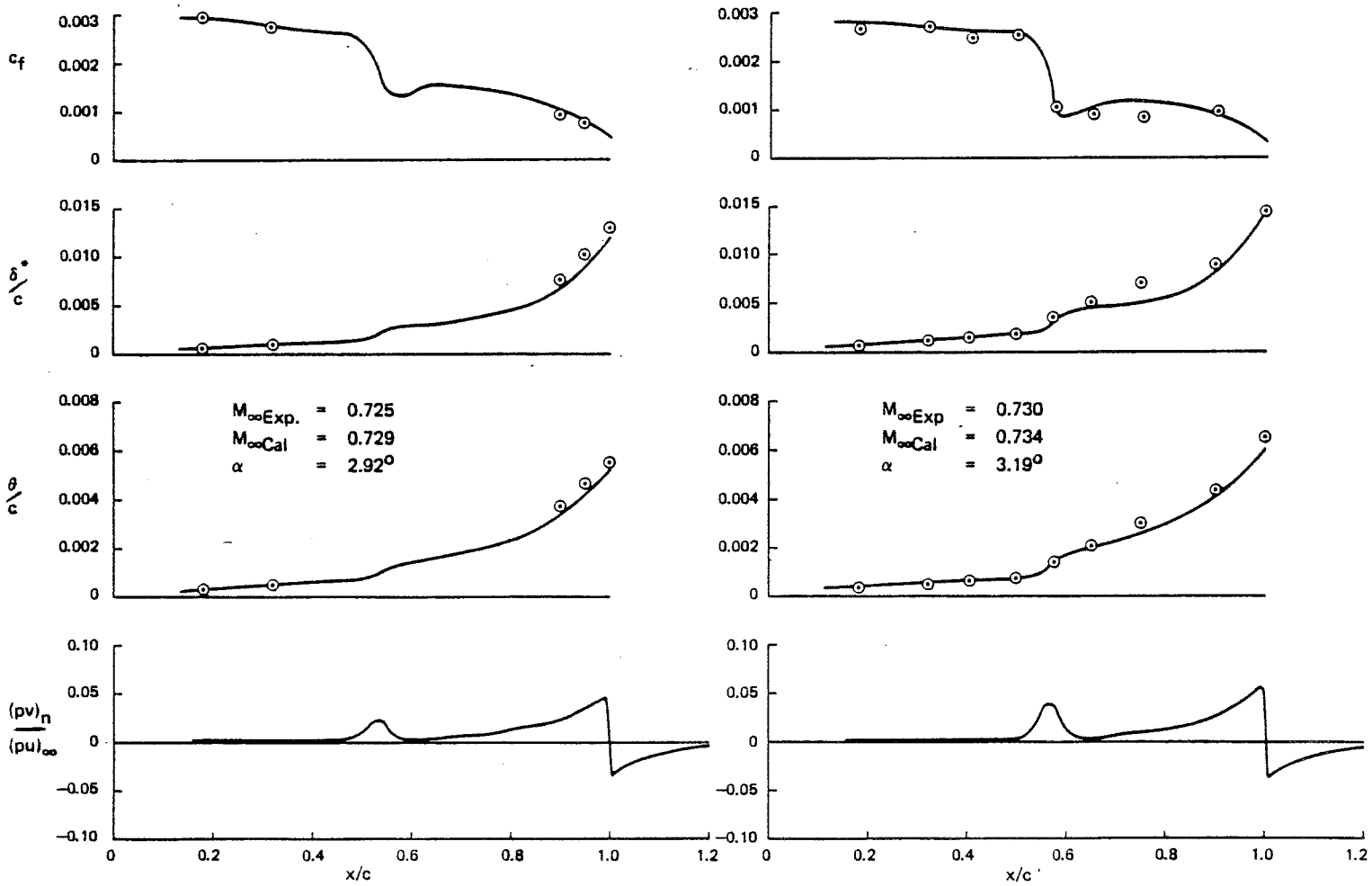
c_f
δ^*/c
θ/c
$(pv)_n/(pu)_\infty$
$M_{\infty Exp.}$ = 0.725
$M_{\infty Cal}$ = 0.729
α = 2.92°
$M_{\infty Exp}$ = 0.730
$M_{\infty Cal}$ = 0.734
α = 3.19°
x/c

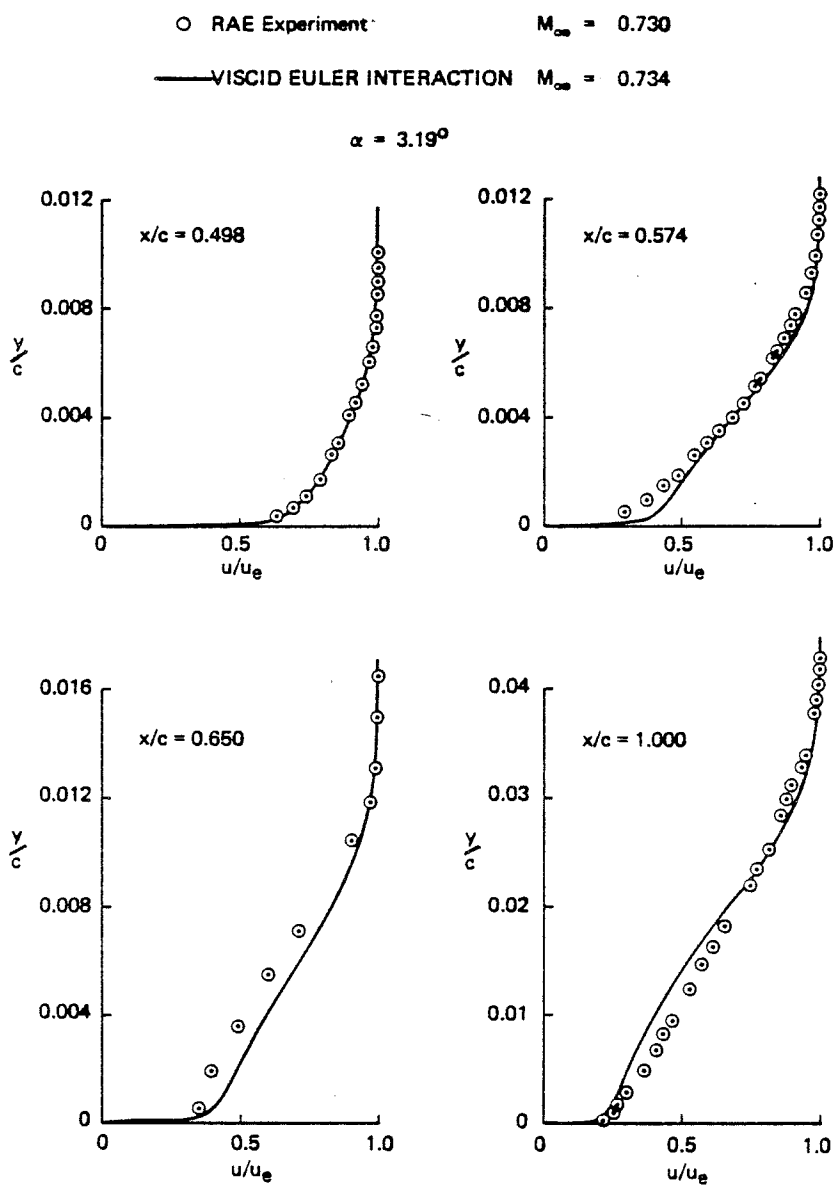

VELOCITY PROFILES

Fig. 22

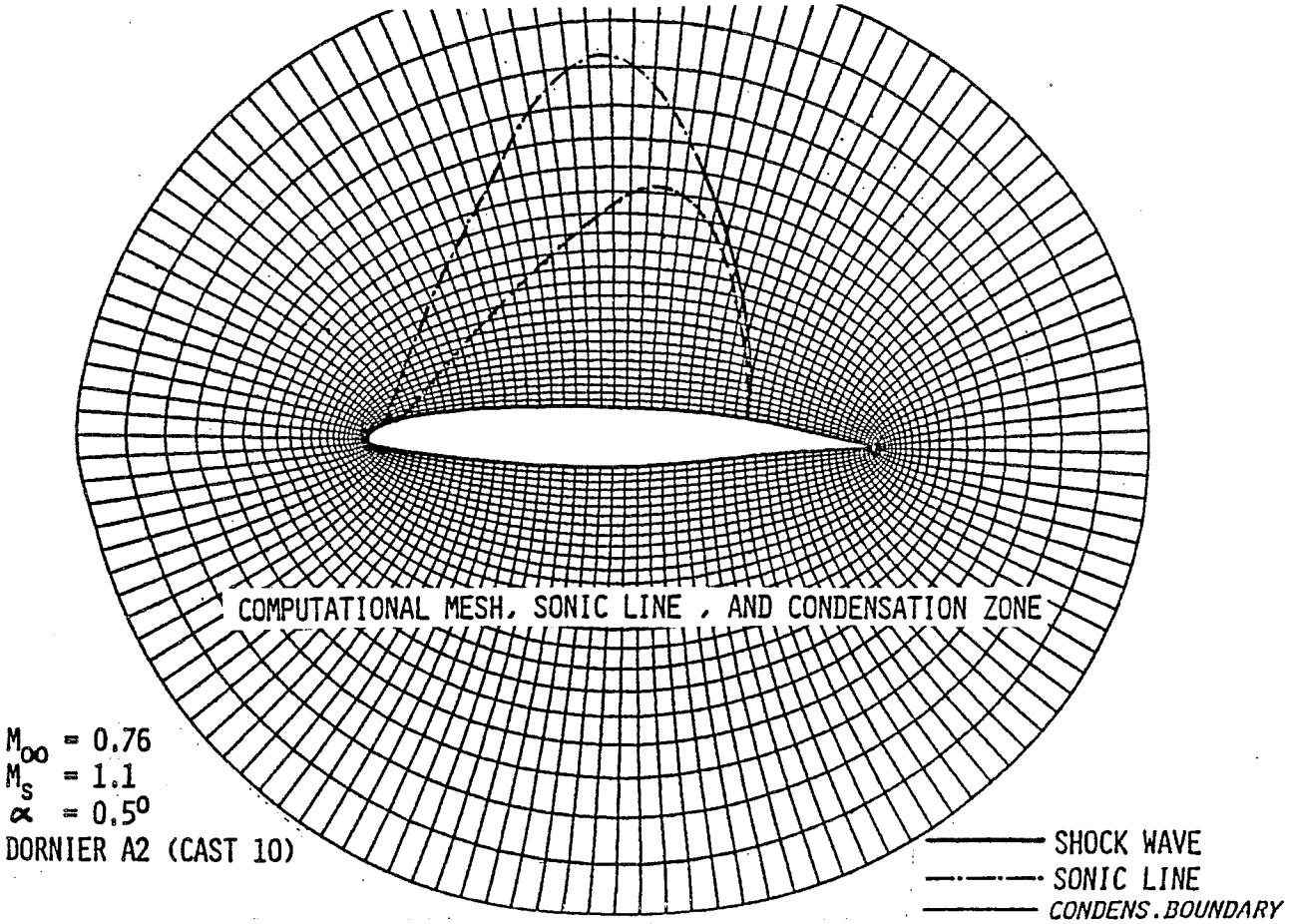

Fig. 23

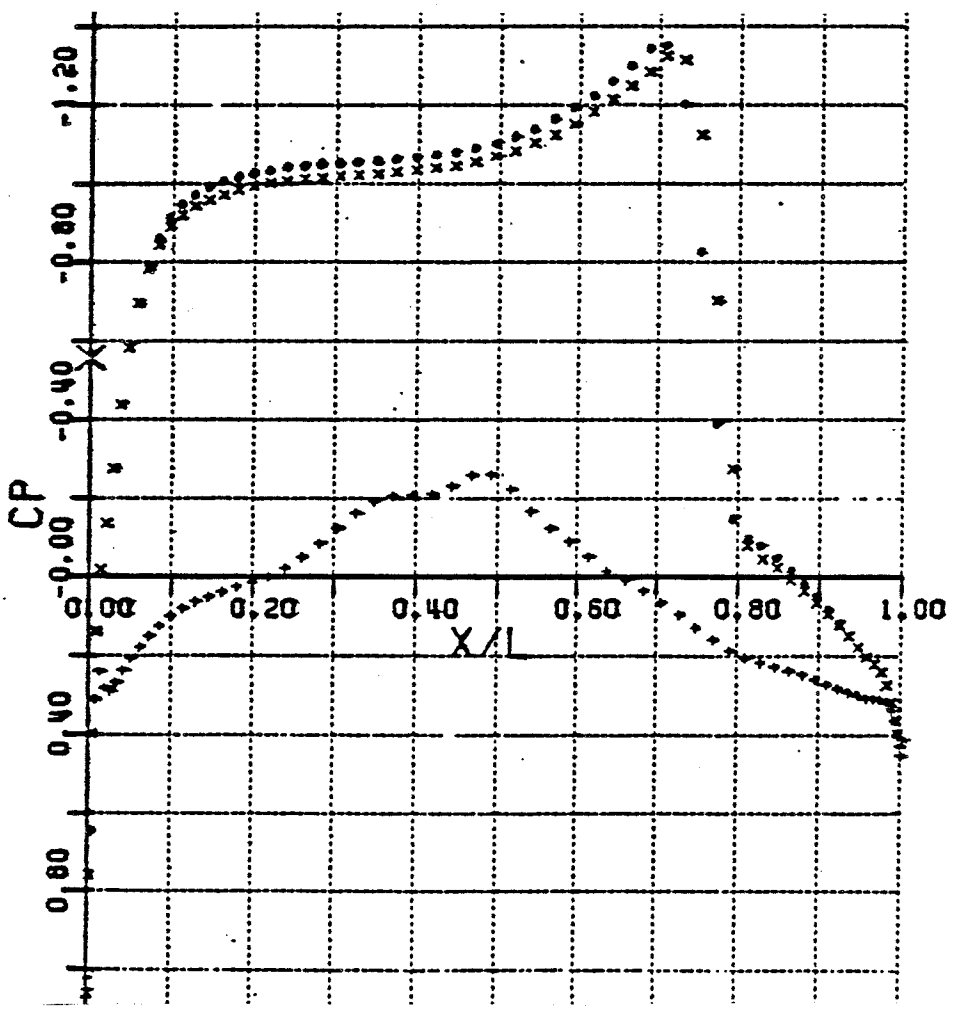

CL= 0.798626 CD= 0.026000 CM= 0.191090

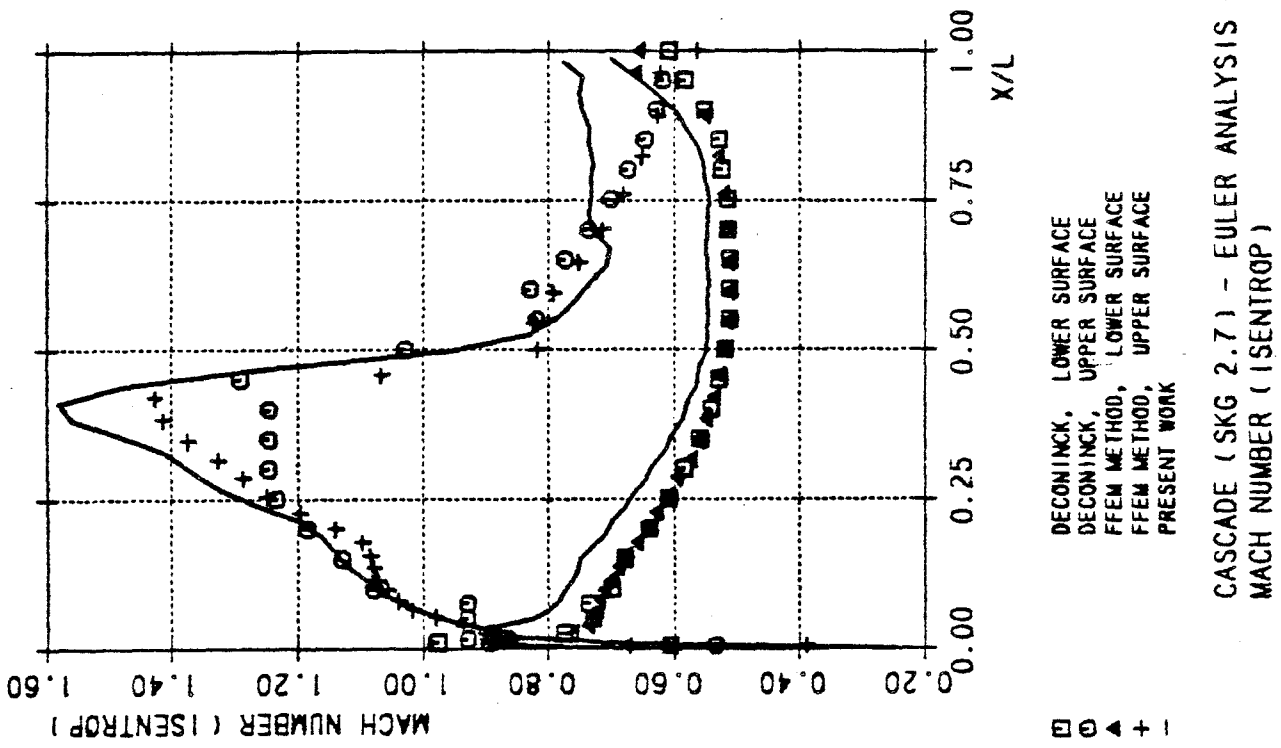
MACH NUMBER (ISENTROP)
0.20
0.40
0.60
0.80
1.00
1.20
1.40
1.60
0.00
0.25
0.50
0.75
1.00
X/L
DECONINCK, LOWER SURFACE
DECONINCK, UPPER SURFACE
FFEM METHOD, LOWER SURFACE
FFEM METHOD, UPPER SURFACE
PRESENT WORK
CASCADE (SKG 2.7) - EULER ANALYSIS -
MACH NUMBER (ISENTROP)

Fig. 24

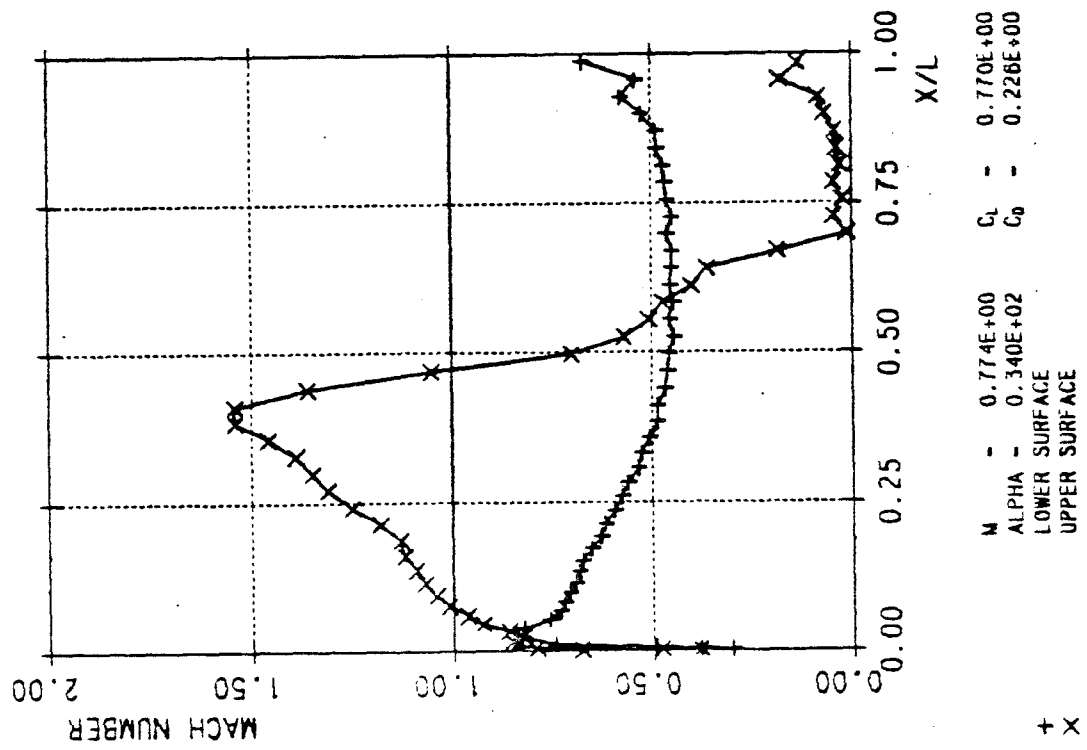
MACH NUMBER
0.00
0.50
1.00
1.50
2.00
0.00
0.25
0.50
0.75
1.00
X/L
M - 0.774E+00
ALPHA - 0.340E+02
LOWER SURFACE
UPPER SURFACE
CL - 0.770E+00
CD - 0.226E+00
CASCADE (SKG 2.7) - EULER ANALYSIS -
MACH NUMBER

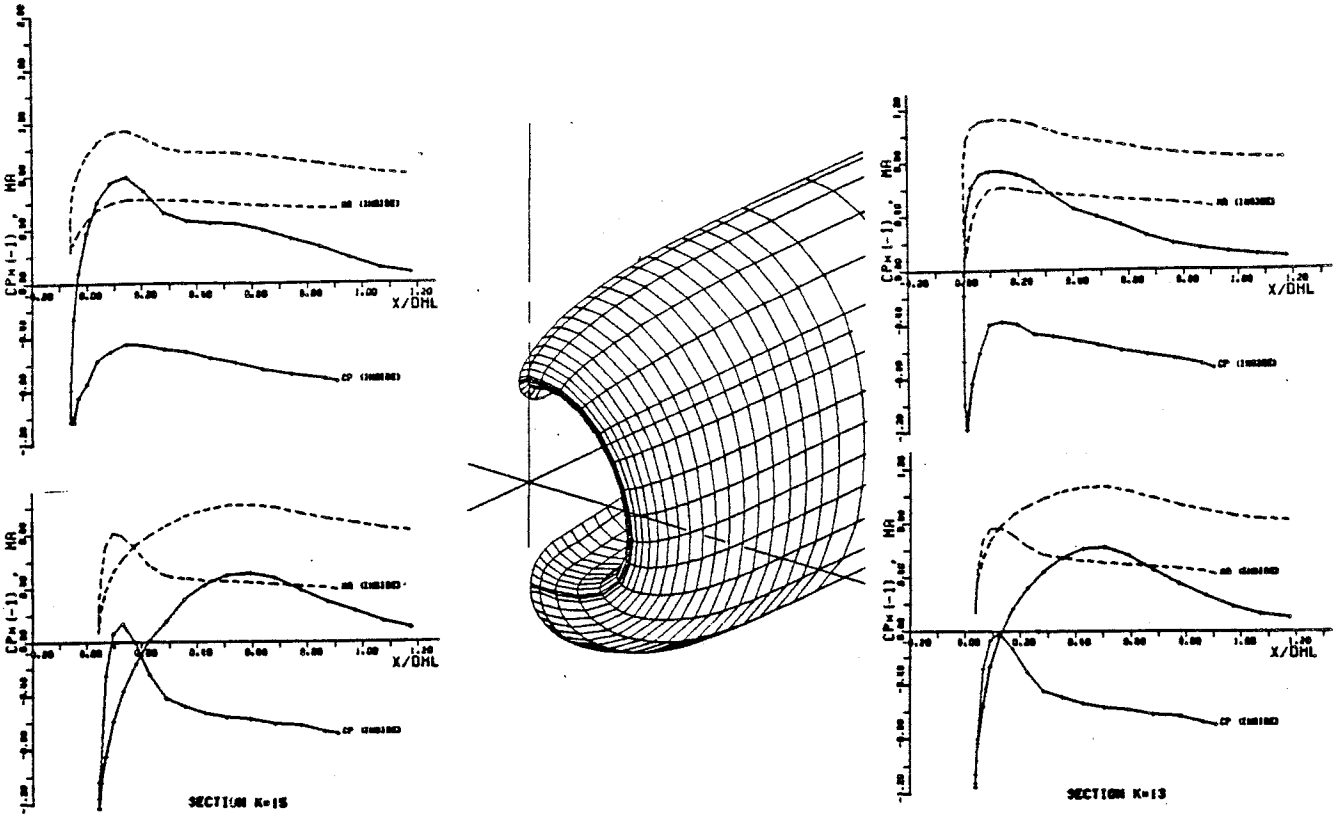

Fig. 25

DORNIER

PRESSURES ON 3-D INLET
AS EULER SOLUTION

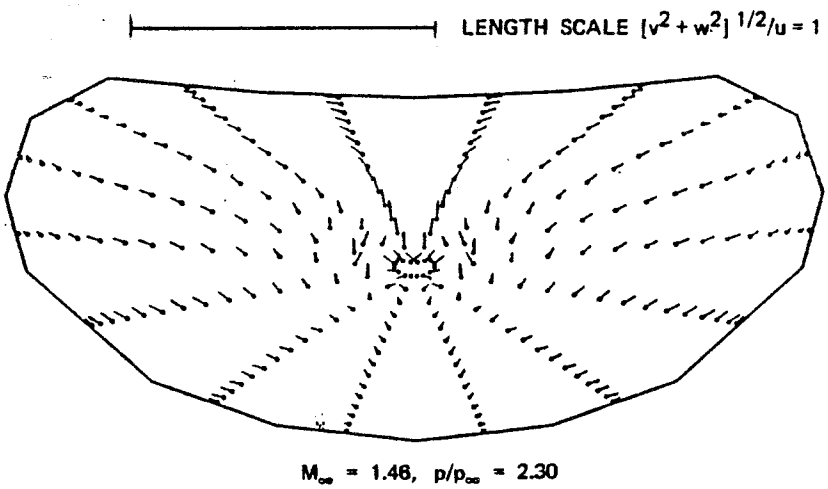

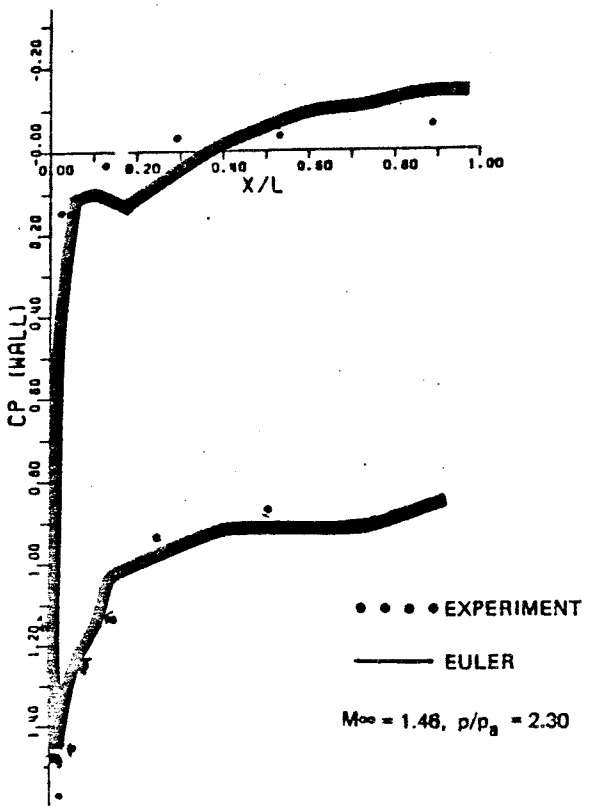

Fig. 26

SUPERSONIC INLET DORNIER EM1

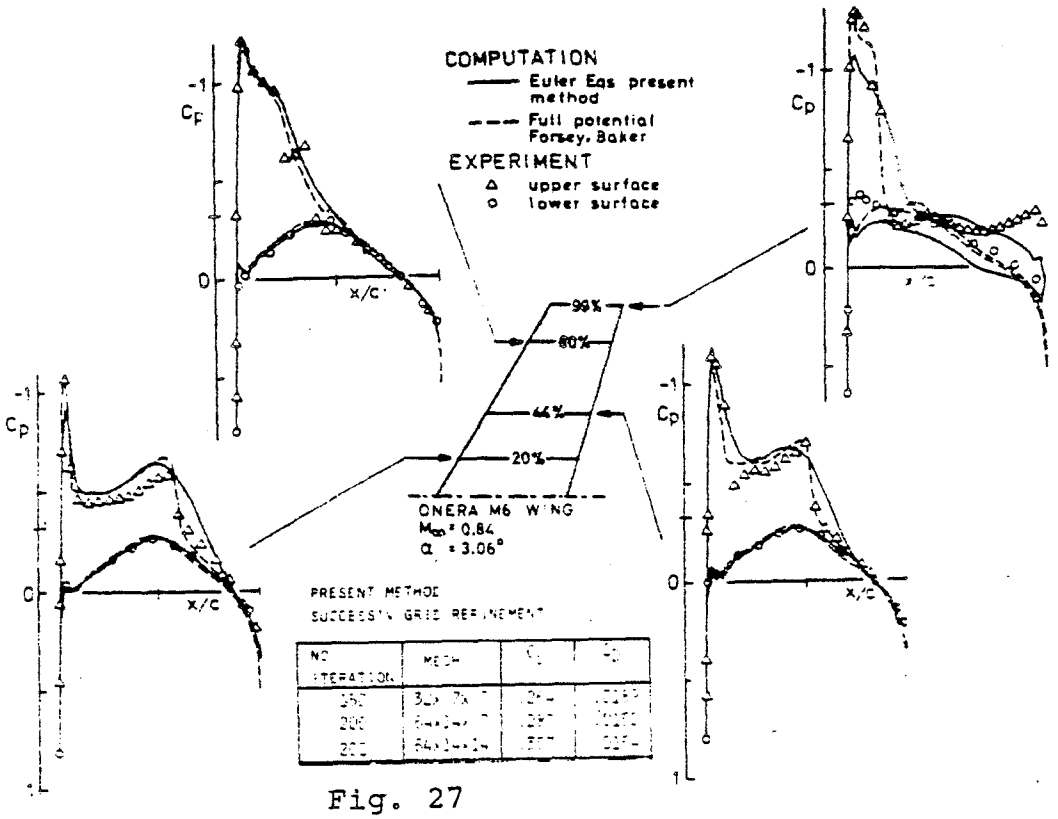

Fig. 27

Comparison of computed and measured pressure coefficients c_p on ONERA M6 wing. $M_\infty = 0.84$ $\alpha = 3.06°$.

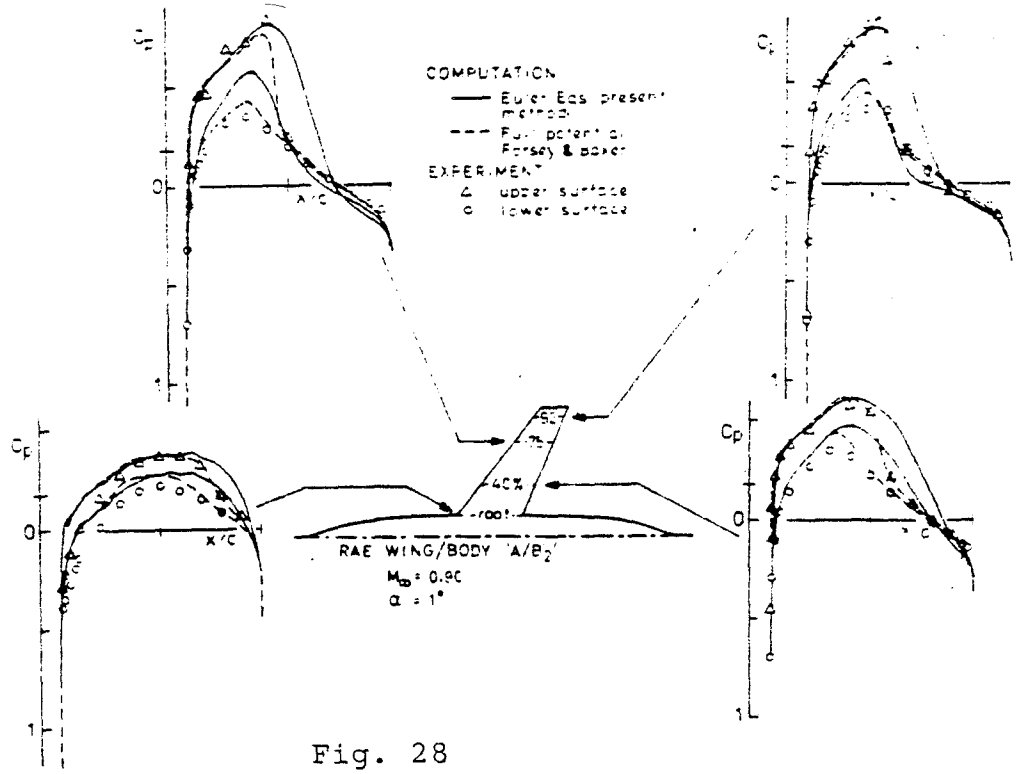

Fig. 28

Comparison of computed and measured pressure coefficients c_p on the RAE A/b_2 wing/body combination. $M_\infty = 0.90$ $\alpha = 1°$.

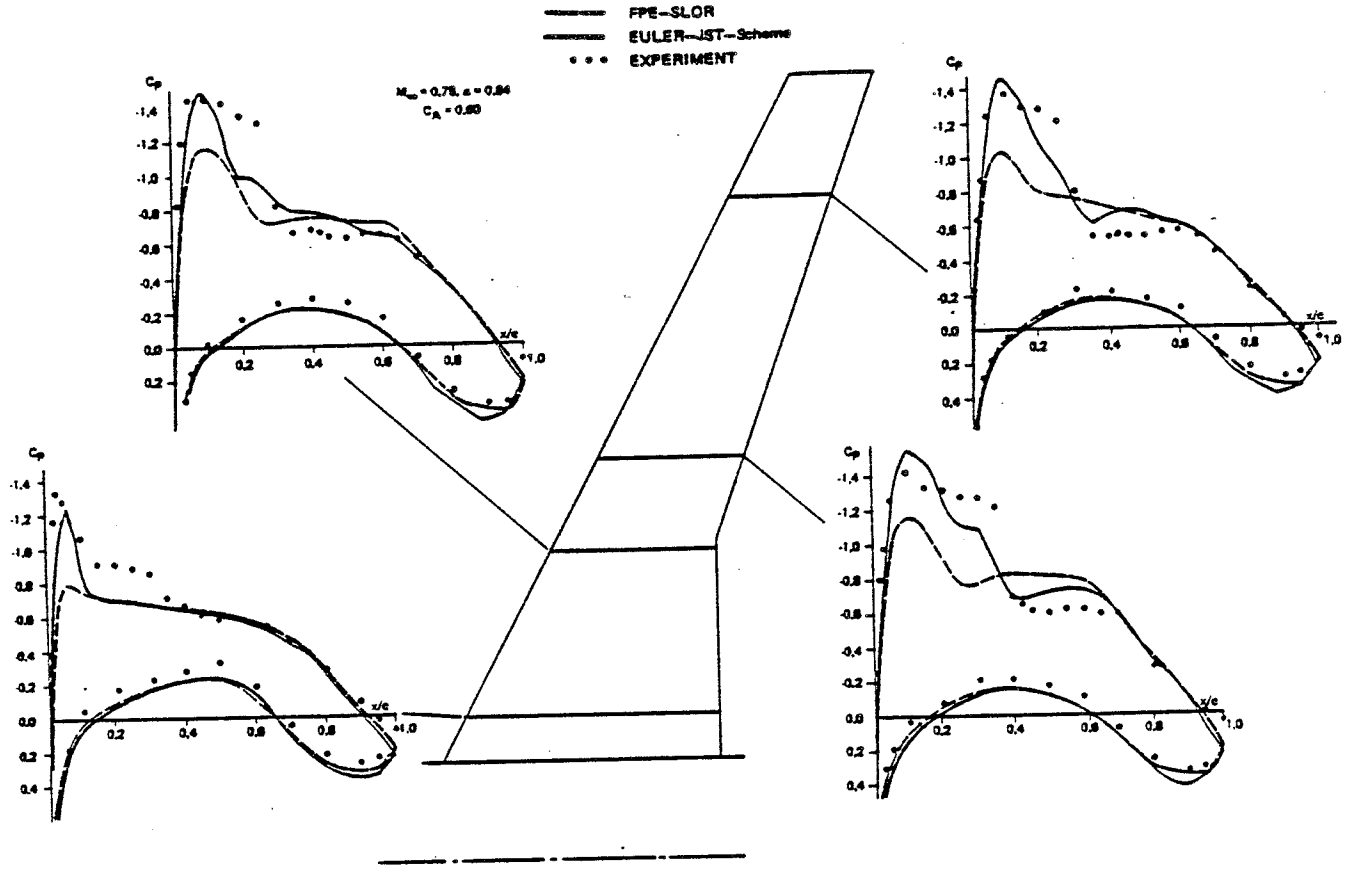

Fig. 30

Comparison of Euler and Full Potential Solution Against Experimental Data for the DFVLR-F4 Wing-Body Combination.

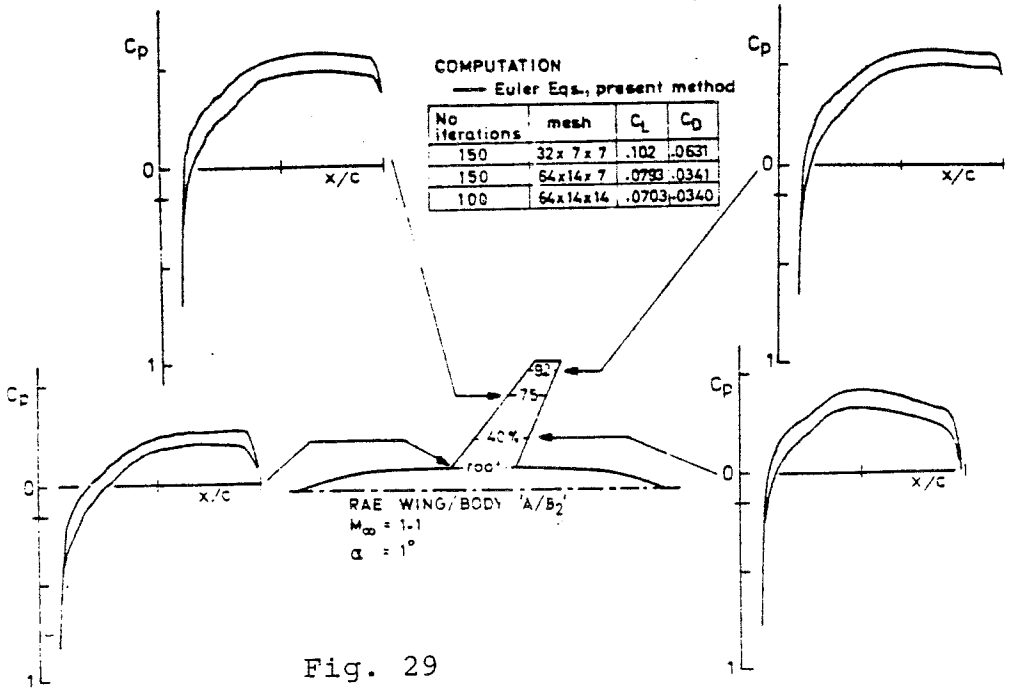

Fig. 29

Computed pressure coefficients c_p on the RAE A/B_2 combination in supersonic flow. $M_\infty = 1.1$ $\alpha = 1^C$.

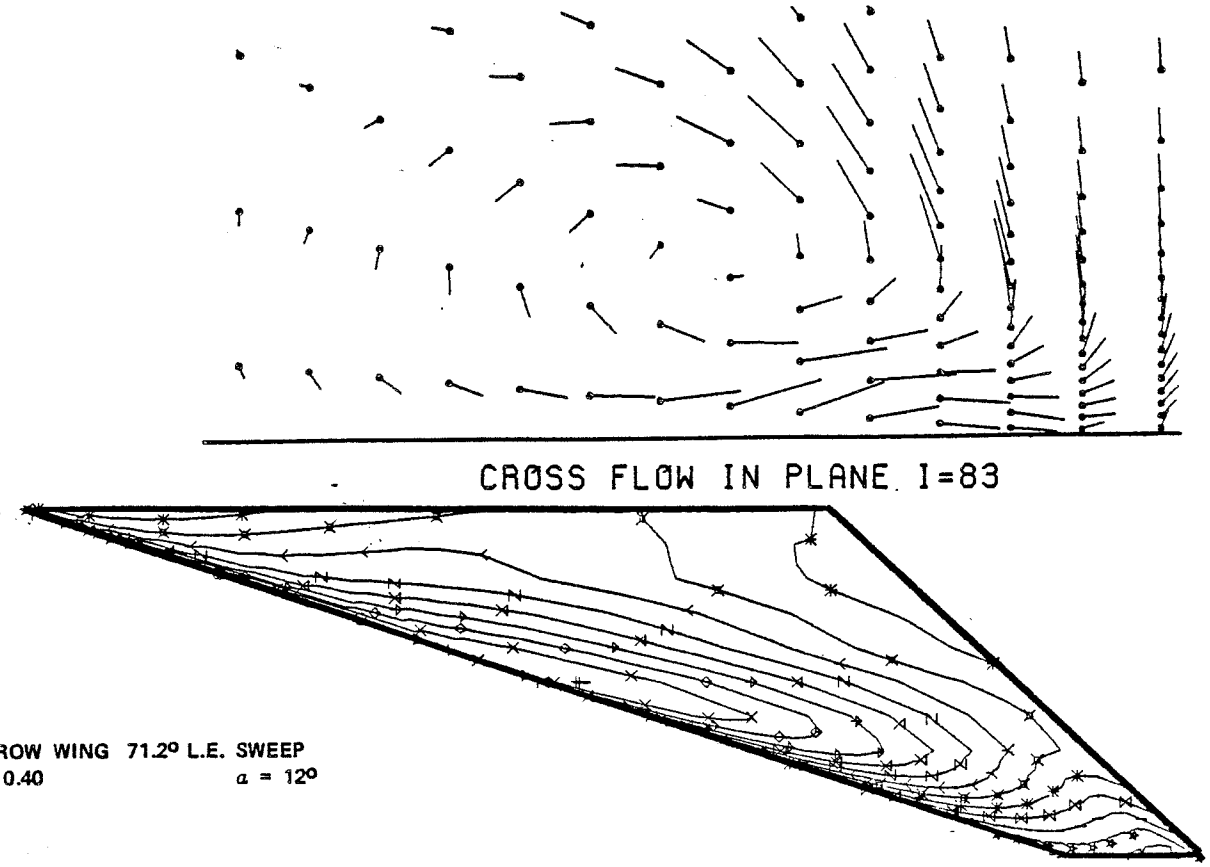

Fig. 31

DORNIER

LEADING EDGE VORTEX FLOW
AS EULER SOLUTION

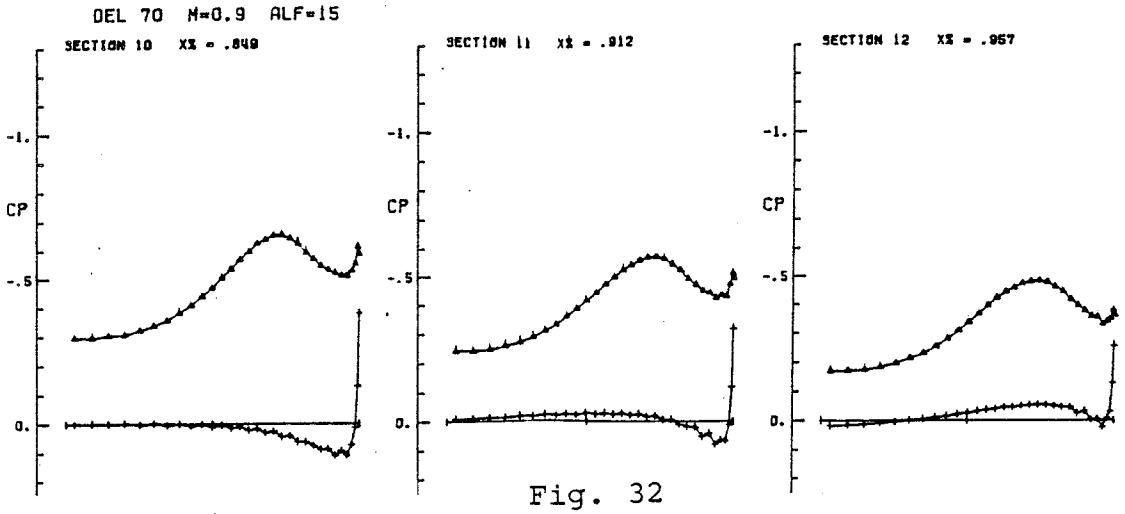

Fig. 32

DELTA WING